Cell

Light modulates glucose metabolism by a retina-hypothalamus-brown adipose tissue axis

Graphical abstract

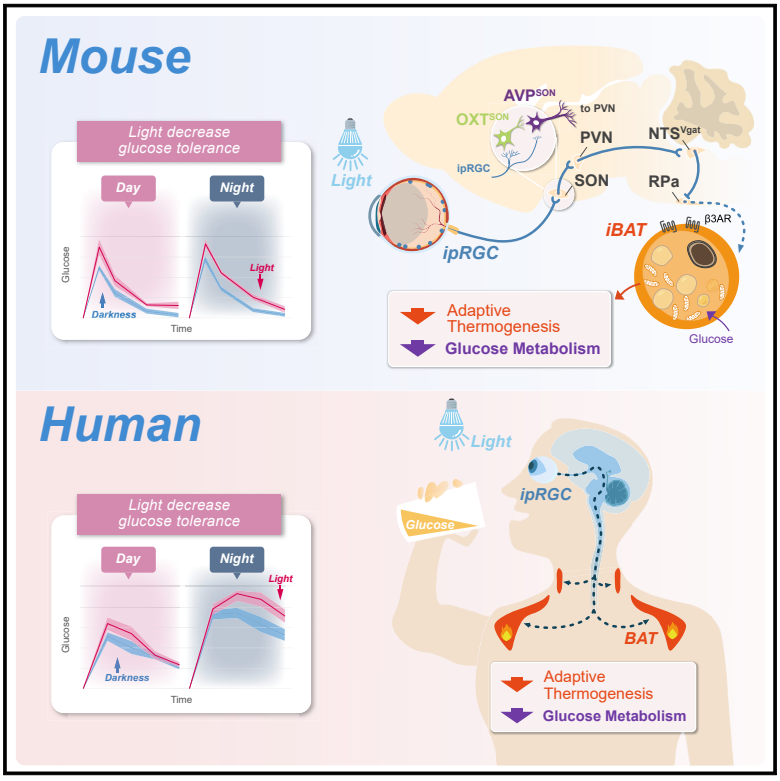

Highlights

- Photoreception of ipRGCs mediates light modulation of glucose tolerance (GT) in mice
- Hypothalamic supraoptic nucleus is essential for light modulation of GT in mice
- Light modulates GT via a neuro circuit that alters adaptive thermogenesis in mice
- Light modulates human GT at the temperature where brown adipose tissue is active

Authors

Jian-Jun Meng, Jia-Wei Shen, Guang Li, ..., Yu-Qian Ma, Huan Zhao, Tian Xue

Correspondence

xuetian@ustc.edu.cn

In brief

Identification of the neuro circuit connecting photoreception to adaptive thermogenesis in brown adipose tissue maps out the biological path mediating the effect of light on glucose metabolism, suggesting potential avenues for managing unintended consequences on metabolic homeostasis by light exposure.

Meng et al., 2023, Cell *186*, 398–412
January 19, 2023
https://doi.org/10.1016/j.cell.2022.12.024

CellPress

CellPress

Cell

Article

Light modulates glucose metabolism by a retina-hypothalamus-brown adipose tissue axis

Jian-Jun Meng,[1,4] Jia-Wei Shen,[1,4] Guang Li,[1] Chang-Jie Ouyang,[1] Jia-Xi Hu,[1] Zi-Shuo Li,[1] Hang Zhao,[1] Yi-Ming Shi,[1] Mei Zhang,[1] Rong Liu,[1] Ju-Tao Chen,[1] Yu-Qian Ma,[1] Huan Zhao,[2] and Tian Xue[1,3,5,*]

[1]Hefei National Research Center for Physical Sciences at the Microscale, CAS Key Laboratory of Brain Function and Disease, Biomedical Sciences and Health Laboratory of Anhui Province, School of Life Sciences, Division of Life Sciences and Medicine, University of Science and Technology of China, Hefei 230026, China

[2]College of Biology, Food and Environment, Hefei University, Hefei 230601, China

[3]Center for Excellence in Brain Science and Intelligence Technology, Chinese Academy of Sciences, Shanghai 200031, China

[4]These authors contributed equally

[5]Lead contact

*Correspondence: xuetian@ustc.edu.cn

https://doi.org/10.1016/j.cell.2022.12.024

SUMMARY

Public health studies indicate that artificial light is a high-risk factor for metabolic disorders. However, the neural mechanism underlying metabolic modulation by light remains elusive. Here, we found that light can acutely decrease glucose tolerance (GT) in mice by activation of intrinsically photosensitive retinal ganglion cells (ipRGCs) innervating the hypothalamic supraoptic nucleus (SON). Vasopressin neurons in the SON project to the paraventricular nucleus, then to the GABAergic neurons in the solitary tract nucleus, and eventually to brown adipose tissue (BAT). Light activation of this neural circuit directly blocks adaptive thermogenesis in BAT, thereby decreasing GT. In humans, light also modulates GT at the temperature where BAT is active. Thus, our work unveils a retina-SON-BAT axis that mediates the effect of light on glucose metabolism, which may explain the connection between artificial light and metabolic dysregulation, suggesting a potential prevention and treatment strategy for managing glucose metabolic disorders.

INTRODUCTION

For life on earth, light is one of the most prominent environmental factors. In mammals, photoreception relies mainly on retinal photoreceptors. Apart from activating conventional rod and cone photoreceptors, which are responsible for image-forming vision, light can also directly activate melanopsin-expressing intrinsically photosensitive retinal ganglion cells (ipRGCs)[1] innervating multiple brain areas, such as the olivary pretectal nuclei, suprachiasmatic nucleus (SCN), preoptic area, and dorsal perihabenular nucleus for controlling the pupillary light reflex (PLR),[2,3] circadian rhythms,[4] sleep,[5,6] mood, and cognitive functions,[7–9] respectively.

Driven by the imperative of survival, mammals have developed precise and complicated regulatory networks for the constant surveillance and dynamic control of glucose metabolism.[10,11] Proper regulation of glucose metabolism demands timely and dynamic modulation in response to environmental factors. Epidemiologic studies have found that artificial light is among the high-risk factors for metabolic diseases such as diabetes and obesity.[12,13] Animal studies have shown that disrupting the circadian rhythm by varying light patterns can affect metabolism.[14,15] For example, weeks-long exposure to abnormal light at night is known to alter internal hormonal rhythms through circadian dysregulation[16–18] and to thereby influence glucose metabolism.[19,20] However, these studies could not unambiguously separate the contributions of light versus circadian rhythm. A recent study[21] observed that perturbed glucose metabolism in a chronic jetlag mouse model was light-intensity dependent, hinting that light might be able to directly modulate glucometabolism.

Here, we present evidence that the hypothalamus supraoptic nucleus (SON) is critical for the effect of light on glucose metabolism. We further show that activation of the ipRGC-SON pathway, which continues to excite paraventricular nucleus (PVN) neurons projecting to GABAergic neurons in the solitary tract nucleus (NTS), blocks adaptive thermogenesis in brown adipose tissue (BAT) through β3-adrenergic signaling, leading to decreased glucose tolerance (GT). Consistent with these findings, light also decreases glucose metabolism in human volunteers, a process in which BAT thermogenesis plays a permissive role.

RESULTS

The ipRGCs are required for the light modulation of GT

To determine the effect of light on glucose metabolism, we kept animals under the standard photoperiods (12/12: light/dark) and then performed an intraperitoneal (i.p.) glucose tolerance test

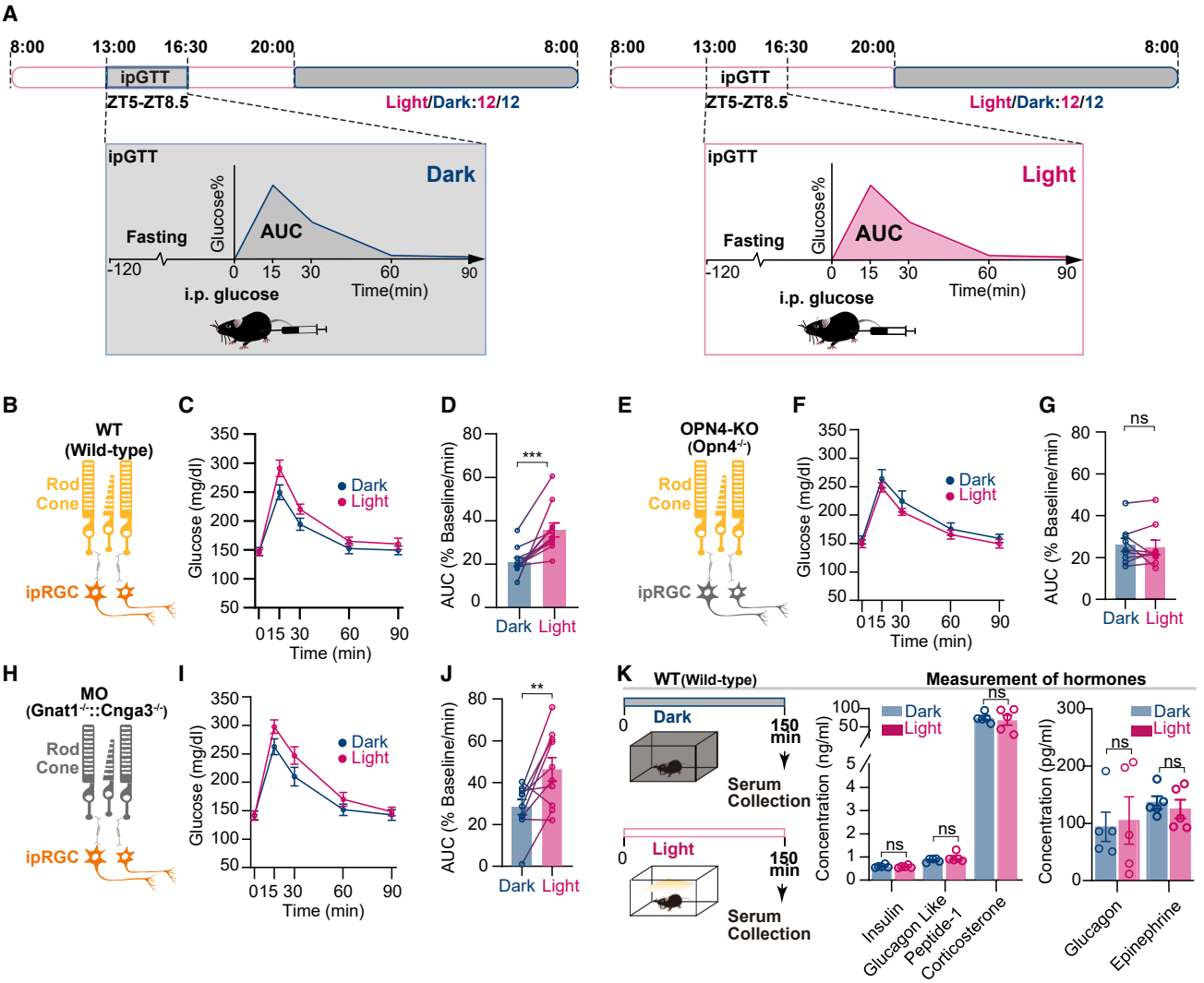

Figure 1. Light decreases GT by ipRGCs

(A) Schematic of the intraperitoneal glucose tolerance testing (IPGTT, 1-g/kg glucose; see STAR Methods) in light and dark conditions during daytime (ZT5–8.5).

(B–D) Illustration of wild-type (WT) retina with intact rods, cones, and ipRGCs (B), the blood glucose levels (C), and AUC data for GT evaluation. Light exposure decreased GT, as indicated by significantly elevated AUC values (D), n = 11 mice. Two-tailed paired t test.

(E–G) Illustration of OPN4-knockout (OPN4-KO: *Gnat1*$^{+/+}$; *Cnga3*$^{+/+}$; *Opn4*$^{-/-}$) retina lacking ipRGC (OPN4) photoreception (E). The blood glucose levels (F). GT was not altered between light/dark conditions (G), n = 9 mice. Two-tailed paired t test.

(H–J) Schematic of melanopsin-only (MO: *Gnat1*$^{-/-}$; *Cnga3*$^{-/-}$; *Opn4*$^{+/+}$) retina lacking rod/cone photoreception (H). The blood glucose levels (I). Light exposure decreased GT (J), n = 10 mice. Two-tailed paired t test.

(K) Experimental procedure for measuring glucometabolism-relevant hormones between light/dark conditions (left). These hormones were not altered between light/dark conditions (middle and right). n = 5 mice/group. Two-tailed non-paired t test.

*p < 0.05, **p < 0.01, and ***p < 0.001. Data were presented as mean ± SEM.

See also Figure S1.

(IPGTT, 1g/kg glucose) during a 3.5 h diurnal window (zeitgeber time ZT5–8.5, Figure 1A) with or without light (white LED light unless otherwise stated, Figure S1K; Table 1). This protocol did not disrupt locomotor activities as shown in actograms (Figure S1A). After 2 h of fasting, we measured blood glucose levels at rest (time 0, when mice had been subjected to dark/light for 2 h) and at 15, 30, 60, and 90 min following the intraperitoneal (i.p.) glucose injection, and we quantified the GT as the area under curve (AUC). Wild-type (WT) mice tested in dark conditions exhibited a notably lower AUC (indicating an increased GT), compared with those tested in light (Figures 1B–1D). This light-mediated decrease of GT was neither due to insulin intolerance nor to altered basal blood glucose levels (Figures S1C and S1J).

Next, the IPGTT was performed on mice under natural sunlight or blue or red LED light (Figure S1L). A higher AUC (decreased GT) was observed in both natural sunlight and blue light compared with dark conditions, whereas red light exposure had no observable effect (Figure S1B). We measured the spectral

Table 1. Characteristics of the LEDs used in experiment

Parameters	Total photon numbers (photons/μm^2.s)	Equivalent intensity to 480 nm (photons/μm^2.s)
sunlight	9.39×10^6	1.93×10^6
blue	2.14×10^6	1.86×10^6
red	2.01×10^6	5.68×10^3
white	1.67×10^6	4.68×10^5

Note: Light intensity equal to 480 nm (peak sensitivity of melanopsin). Equivalent intensities were calculated by using normalized spectral sensitivity of OPN4.

power distributions of these light sources and converted them into equivalent 480-nm monochromic light intensities (Table 1), based on the mice melanopsin action spectrum with peak at 480 nm.[22] These equivalent 480-nm light intensities reflect these light sources' capabilities to effectively activate ipRGCs.[23] Indeed, although the original photon intensity (total photon numbers) of red light was comparable to that of blue light or sunlight, the equivalent number of photons at 480 nm for red light was two to three orders of magnitudes lower than that for blue or sunlight (Table 1). The intensities of sunlight, white LED light, and blue LED light were all sufficient to activate ipRGCs,[23] indicated by prominent pupil contraction in *Opn4*$^{+/+}$; *Pde6b*$^{rd1/rd1}$; *Cone*^{DTA} mice (which only have ipRGC photoreception) (Figures S1K and S1L). These results suggest that light regulates GT when it can effectively activate ipRGCs.

Next, to determine which type of photoreceptor mediates the effect of light on GT, we performed IPGTTs in mice lacking ipRGC photoreception due to loss of function (LoF) of *Opn4*, which encodes melanopsin (OPN4-KO: *Opn4*$^{-/-}$, Figure 1E), and mice lacking rod and cone photoreception (melanopsin-only [MO]: *Gnat1*$^{-/-}$, *Cnga3*$^{-/-}$, *Opn4*$^{+/+}$, Figure 1H) in light or dark conditions. WT and MO mice exhibited a higher AUC (decreased GT) in light when compared with AUC in darkness (Figures 1I and 1J). Conversely, the AUC of OPN4-KO mice (Figures 1F and 1G) was not affected by light, indicating that ipRGCs are the major photoreceptors responsible for the effect of light on GT. We also performed IPGTTs during nighttime (ZT13–16.5). AUC in darkness was found to be lower (increased GT) than AUC measured when there was light (Figures S1D–S1G), comparable to our findings during daytime, confirming that the effect of light on GT was independent of the circadian phase (day or night).

We further screened for light-induced changes of hormones and nutrients involved in glucose metabolism (insulin, glucagon like peptide-1, corticosterone, glucagon, epinephrine, lactate, non-esterified fatty acids, norepinephrine, ghrelin, orexin A, growth hormone, cholecystokinin, leucine, 4-OH-isoleucine, valine, and cholesterol) and found that all those examined were unaltered (Figures 1K, S1H, and S1I). These data indicate that there might be a direct neural circuit mediating light modulation of GT.

An ipRGC-hypothalamic SON projection mediates the light modulation of GT

IpRGCs are known to directly project to the hypothalamic region,[24] a crucial hub in regulation of metabolism.[25] Among all the hypothalamic nuclei receiving ipRGCs inputs, the SCN (central circadian pacemaker) and the SON are the most heavily innervated.[24] This was confirmed in *Opn4-Cre* mice (for selective labeling of ipRGCs) by performing anterograde viral tracing, using monocular injections of AAV2/2-DIO-ChR2-EYFP (Figures 2A and 2B), and retrograde tracing from the SCN or SON, using AAV2/2Retro-DIO-ChETA-EYFP (Figures 2C–2F). In addition, substantial c-Fos expression in the SCN and SON, following light stimulation, was detected (Figures S2A and S2B), which further verified that ipRGCs provide extensive inputs to the SCN and SON.

We separately probed the SCN and SON with an excitotoxic lesion to evaluate their contributions to the light-mediated decrease of GT. The SCN lesion abolished the circadian rhythm yet had no effect on the light-induced difference in AUC. Surprisingly, SON lesion completely prevented light modulation of GT while leaving the circadian rhythm intact (Figures 2G, 2H, S2C, and S2H). We further employed *Opn4*$^{f/f}$ mice, a genetically engineered strain that allows Cre-dependent knock out of melanopsin.[26] Using these mice, we achieved specific ablation of photoreception in SON-innervating ipRGCs (OPN4-KO^{SON}) and SCN-innervating ipRGCs (OPN4-KO^{SCN}) by injecting AAV2/2Retro-Cre into the SON and SCN areas, respectively. The AUCs for OPN4-KO^{SCN} mice and control mice (*Opn4*$^{f/f}$) were higher in light than in darkness. In the OPN4-KO^{SON} mice, on the other hand, the difference in AUCs between light and dark conditions was abolished (Figures 2I, S2D, S2E, and S2H), suggesting that light no longer affects GT in these animals. These results indicate that the SON, but not SCN, plays a key role in the effect of light on GT.

To evaluate the percentage of ipRGCs in SON-innervating RGCs, we delivered AAV2/2Retro-GFP into SON in WT mice. There were 121.3 ± 7.5 SON-innervating RGCs per retina (GFP positive) (Figure S2F). The retrograde tracing experiment showed that overall numbers of SON-innervating ipRGCs in *Opn4-Cre* mice was 101.3 ± 5.0 (Figure 2F). Thus, the percentage of SON-innervating ipRGCs was about ~83%, supporting the notion that ipRGCs carry major retinal inputs to the SON.

We next chemogenetically manipulated the SON-projecting ipRGCs to assess their roles in light modulation of GT. AAV2/2Retro-Cre was delivered into the SON, by injecting either an excitatory or inhibitory chemogenetic virus (excitatory: AAV2/2-DIO-hM3Dq-mCherry, inhibitory: AAV2/2-DIO-hM4Di-mCherry, control: AAV2/2-DIO-mCherry) into the vitreous chamber of the eyes. Approximately 70% of retrogradely labeled (mCherry-positive) RGCs were melanopsin immunopositive (Figures 2J and 2K). Considering the efficiency of melanopsin antibody, this percentage is reasonable. There are ~117 SON-innervating hM3Dq-mCherry and ~120 SON-innervating hM4Di-mCherry-positive RGCs per retina (Figure S2G), suggesting that most SON-innervating RGCs (121.3 ± 7.5) were infected by chemogenetic virus. Also, 30 min prior to the IPGTT, mice received 2 mg/kg i.p. clozapine-N-oxide (CNO) for tonic activation (hM3Dq) or inhibition (hM4Di) of ipRGCs. We found that both exciting and repressing SON-projecting ipRGCs abolished the light/dark difference in AUC, yet in an opposing fashion. Activation of SON-projecting ipRGCs increased the AUC in darkness to the level observed in light (Figures 2L and S2I); inhibition of

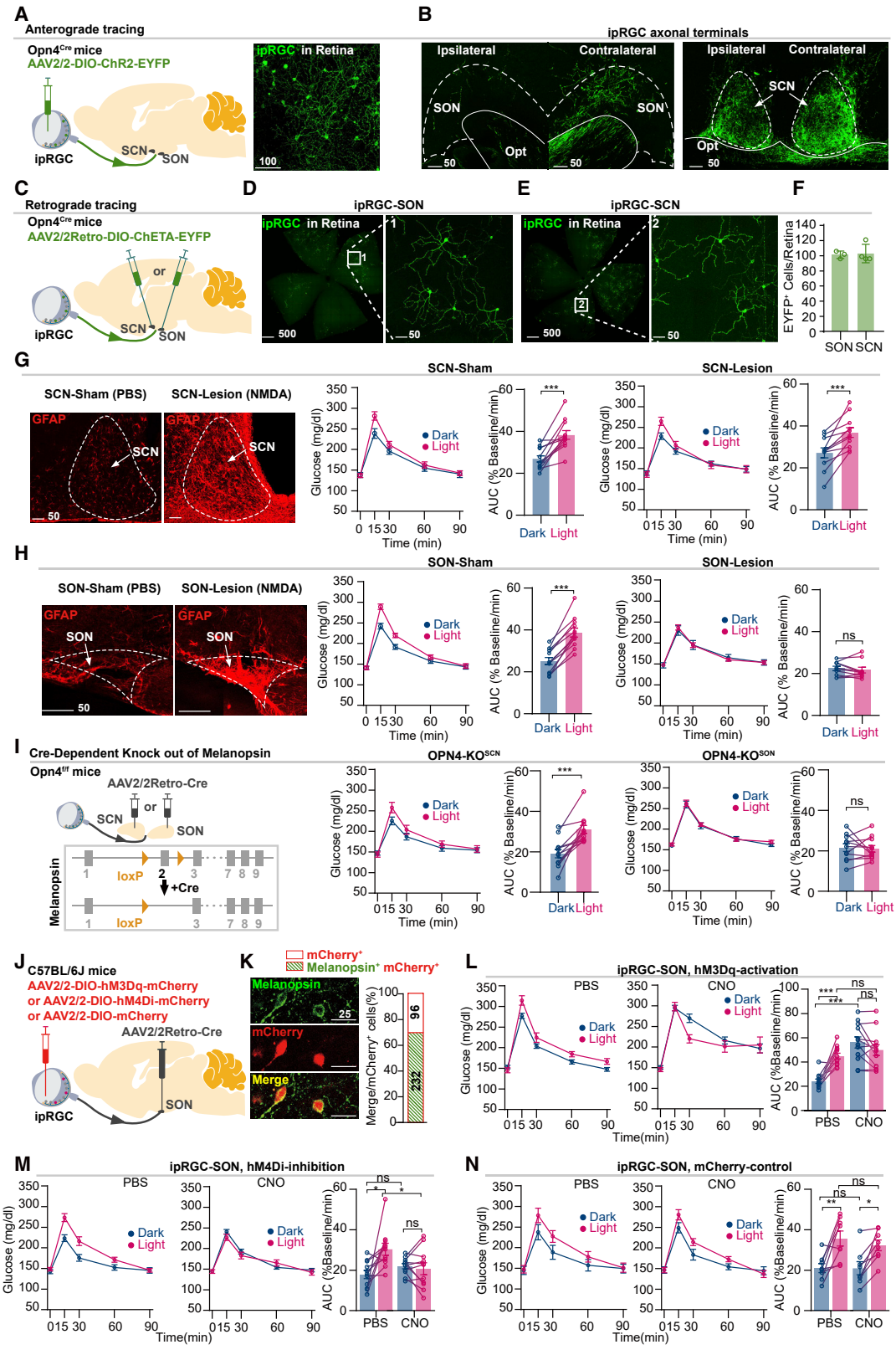

(legend on next page)

SON-projecting ipRGCs, however, reduced the AUC in light to that in darkness (Figures 2M and S2I). These results were consistent with our proposed model in which ipRGC projections to the SON mediate the effect of light on GT. In control animals expressing mCherry, the effects of light on GT were similar regardless of whether they received PBS or CNO treatment, which ruled out non-specific actions of CNO (Figures 2N and S2I).

The SON^{AVP}-PVN projection is necessary for light modulation of GT

The SON mainly harbors two neuronal subtypes, vasopressin (AVP) and oxytocin (OXT) neurons. Trans-synaptic retrograde tracing was conducted by introducing a modified rabies virus (RV-EnvA-ΔG-mRuby3) and helper viruses (AAV2/5-DIO-RVG and AAV2/5-DIO-H2B-EGFP-T2A-TVA) into *Oxt-Cre* and *Avp-Cre* mice, which enabled labeling of input neurons that synapse onto SON OXT (SON^{OXT}) and AVP (SON^{AVP}) neurons, respectively (Figures 3A and S3A). We found that both SON^{OXT} and SON^{AVP} neurons received inputs from ipRGCs with approximately 5-fold more ipRGCs retrogradely labeled from SON^{OXT} than from SON^{AVP} (Figures 3B and 3C). The SON^{OXT} and SON^{AVP} neurons were both excited by light (Figures S3B and S3C). We then sought to dissect the contributions of SON^{OXT} and SON^{AVP} neurons to light modulation of GT by performing LoF manipulations (Figure S3D). Chemogenetic inhibition of SON^{OXT} neurons reduced the AUC (increased GT) in light to the level observed in darkness (Figures 3D and S3G). Similar results were also obtained from chemogenetic inhibition of SON^{AVP} neurons (Figures 3E and S3H). These data suggest that both SON^{OXT} and SON^{AVP} neurons are required for light modulation of GT. We hence speculated that there exists a microcircuit within the SON. In fact, we did find substantial reciprocal projections between SON^{AVP} and SON^{OXT} neurons (Figures 3F and 3G). Furthermore, previous reports suggested that OXT or AVP neurons could regulate glucose metabolism[27,28] by releasing these peptides into blood circulation. However, no light/dark differences in the plasma vasopressin and oxytocin levels were observed (Figure S3E).

SON is known to project to the PVN,[29] an important brain area for controlling the metabolism.[30–32] Our retrograde virus tracing further revealed that PVN-projecting neurons in the SON were primarily AVP positive (Figures 3H–3J). We suppressed PVN-innervating SON neurons, using the tetanus toxin (TetTox), and found that the difference in AUC between light and dark conditions was abolished (Figure S3F). We then delivered AAV2/2Retro-FLEX-Flp into the PVN while delivering AAV2/9-fDIO-hM4Di-mCherry into the SON of *Avp-Cre* mice to achieve selective inhibition of PVN-projecting SON^{AVP} neurons. We found that this manipulation prevented the light-mediated decrease in GT and reduced the AUC level in light (Figures 3K and S3I), indicating that SON^{AVP} neurons were the major output neurons from the SON to the PVN in this pathway.

PVN projection to the medulla is required for light modulation of GT

To determine the downstream targets in the pathway for light modulation of GT, we performed anterograde trans-synaptic tracing by injecting scAAV2/1-Cre into the SON and AAV2/9-FLEX-GFP into the PVN, enabling selective GFP expression in SON-innervated PVN neurons. We found dense labeling of GFP-positive axonal terminals in the NTS of the medulla (Figures 4A and 4B), along with sparse signals in the periaqueductal gray and dorsal raphe regions (Figure S4A). Retrogradely modified rabies virus (RV) tracing from NTS-projecting PVN neurons confirmed the synaptic relay of SON-PVN-NTS (Figures 4C and S4B). Furthermore, labeled neurons in the SON were exclusively AVP positive (Figures 4D and 4E), suggesting that SON^{AVP}, but not SON^{OXT},neurons serve as the output neurons innervating the NTS via PVN. We then inhibited the NTS-projecting PVN neurons, through either CNO-induced inactivation or TetTox-mediated synaptic suppression, and found that the AUCs for the CNO and TetTox treatments were lower in light (increased GT) and thus exhibited no light/dark difference (Figures 4F–4H, S4C, and S4H). In addition, we found that NTS-projecting PVN neurons were OXT and brain-derived neurotrophic factor (BDNF) positive (Figures S4D and S4E) and that GABAergic neurons in the NTS received PVN projections (Figure S4F).

The GABAergic NTS neurons are known to innervate the rostral raphe pallidus (RPa), which is involved in regulating the glucose sink properties of BAT.[33,34] Moreover, our tracing experiment also revealed that NTS neurons relaying PVN inputs to the RPa were predominantly GABAergic (Figure 4I). Therefore,

Figure 2. IpRGCs' input to hypothalamic SON mediates light decrease of GT

(A and B) Schematic of anterograde tracing and image of ipRGCs in *Opn4-Cre* mice (A) and their terminals in SON and SCN areas (B).

(C–F) Schematic of the retrograde tracing system used to quantify SON-innervating ipRGCs and SCN-innervating ipRGCs in *Opn4-Cre* mice (C). Images (D) and (E) and quantification (F) of SON-innervating ipRGCs (mean ± SD, 101.3 ± 5.0, n = 3 mice) or SCN-innervating ipRGCs (103 ± 12.1, n = 4 mice).

(G) GFAP labeling outlined the NMDA-induced lesion in SCN. Light exposure decreased GT in SCN-Sham (n = 12) and SCN-lesioned mice (n = 11). Both by two-tailed paired t test.

(H) GFAP labeling outlined the NMDA-induced lesion in SON. Light exposure decreased GT in SON-Sham (n = 12) mice but not in SON-lesioned mice (n = 10). Both by two-tailed paired t test.

(I) Cre-dependent knock out of melanopsin in SON-projecting ipRGCs ($OPN4\text{-}KO^{SON}$) or SCN-projecting ipRGCs ($OPN4\text{-}KO^{SCN}$). Light exposure decreased GT in $OPN4\text{-}KO^{SCN}$ mice (n = 12) but not in $OPN4\text{-}KO^{SON}$ mice (n = 11). Both by two-tailed paired t test.

(J and K) Schematic of ipRGC-SON tracing and of inhibitory or excitatory manipulations of SON-projecting ipRGCs (J). Image of SON-projecting ipRGCs. Arrowhead denotes melanopsin immunofluorescence (green) overlapped with SON-projecting RGCs (red) in retina (K). Percentage (70.0% ± 2.9%) of $ipRGCs^{+}$-$mCherry^{+}$ cells were observed in SON-projecting RGCs ($mCherry^{+}$). n = 3 mice.

(L–N) GT evaluation with CNO-induced activation ([L] n = 12 mice, hM3Dq) and inhibition ([M] n = 11 mice, hM4Di) of ipRGCs-SON pathway, and in control mice ([N] n = 8 mice, mCherry). All by two-way ANOVA, Tukey's post hoc test.

*p < 0.05, **p < 0.01, and ***p < 0.001. Data were represented as mean ± SEM. Scale bars, 100 μm in (A), 50 μm in (B), (D), (E), (G), and (H), and 25 μm in (K). See also Figure S2.

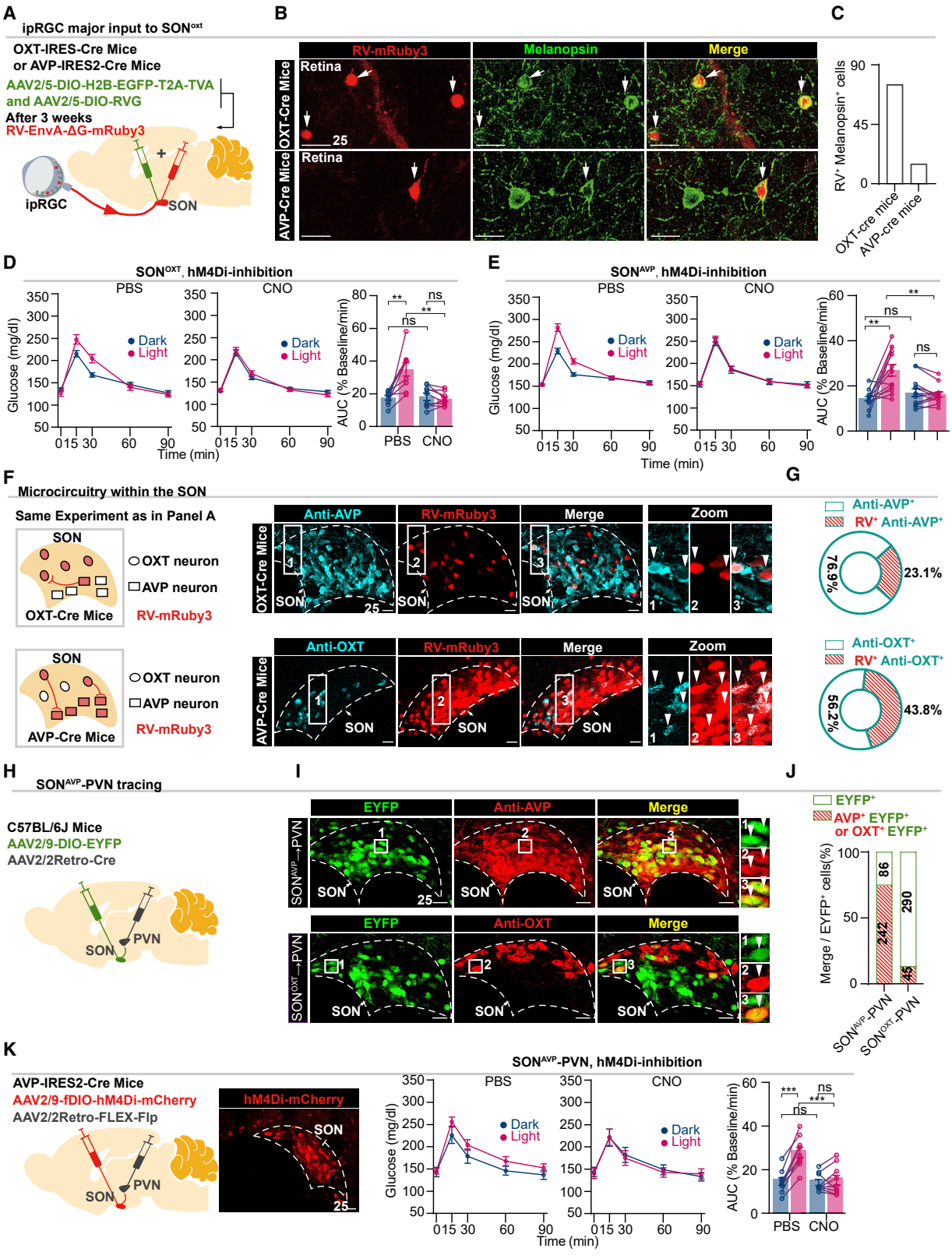

(legend on next page)

to determine whether Rpa-projecting GABAergic neurons in the NTS mediate the decrease of GT in response to light, we injected AAV2/2Retro-FLEX-Flp into the RPa and AAV2/9-fDIO-hM4Di-mCherry into the NTS to chemogenetically inhibit RPa-projecting NTS Vgat (NTS^{Vgat}) neurons in *Vgat-Cre* mice. This manipulation again reversed the effect of light and reduced the AUC in light to the level observed in darkness (Figures 4J, S4G, and S4H). Together, these observations show that light regulates GT via the ipRGC-SON^{OXT}-SON^{AVP}-PVN-NTS^{Vgat}-RPa pathway (Figure 4K).

Light decreases GT by blocking adaptive thermogenesis in BAT

The sympathetic premotor neurons residing within the RPa directly modulate BAT thermogenesis,[33] which is closely associated with blood glucose clearance.[35] We delivered retrograde RFP-expressing pseudorabies virus (PRV) into intrascapular BAT (iBAT) and identified several brain regions, including the SON, PVN, NTS, and Rpa, as upstream hotspots (Figures 5A, 5B, and S5A), establishing an anatomical link between iBAT and the SON-PVN-NTS-RPa pathway.

Next, we examined whether light modulates BAT thermogenesis. In dark conditions, a single glucose injection induced an adaptive change in BAT thermogenesis, with an increase in iBAT surface temperature. Interestingly, light blocked this adaptive thermogenesis (Figures 5C and 5D). Expression of key thermogenic genes in iBAT, including *Ucp1, Pgc1a, Dio2*, was upregulated in dark conditions following glucose loading but was not altered in light conditions (Figure S5C). Given that there is white/beige adipose tissue under the skin surrounding iBAT, we investigated whether light regulation of intrascapular surface temperature was caused by white/beige adipose tissue or iBAT. We made bilateral cuts in five intercostal sympathetic nerve branches subserving iBAT (Figure S5B), as previously described,[36,37] and found that glucose-induced elevation in intrascapular surface temperature was abolished (Figure 5E). Therefore, the increased intrascapular surface temperature is being driven mainly by iBAT, but not by white/beige adipose tissue. These suggest that light does modulate glucose-induced BAT thermogenesis through sympathetic pathway.

We further examined whether this light regulation of BAT thermogenesis caused light modulation of GT. Since it was reported that BAT-mediated adaptive thermogenesis can be restricted by thermoneutrality (~30°C),[38,39] we indeed found that the glucose-induced BAT thermogenesis was abolished at 30°C. We measured GT at 30°C and found that the increased GT observed in darkness was also abolished (Figures 5F and S5J). In addition, treatment with SR59230A (a selective β3-adrenoceptor antagonist, 1 mg/kg i.p.) blocked the BAT-mediated adaptive thermogenesis in darkness (Figure 5G), resembling the light-induced suppression. Importantly, SR59230A also decreased GT in darkness, increasing the dark AUC to that observed in light, mimicking the effect of light on GT (Figures 5H and S5J). Similarly, in β3-adrenergic receptor (β3AR) knockout mice (*Adrb3*$^{-/-}$), AUC did not differ between light and dark conditions (Figures 5I and S5J). The difference in adaptive thermogenesis previously seen when comparing light and dark conditions was again abolished in *Adrb3*$^{-/-}$ mice (Figures 5J and 5K). These results indicate that light blocks BAT-mediated adaptive thermogenesis via β3-adrenergic signaling to decrease GT.

In OPN4-KO mice, iBAT surface temperature was increased in both light and dark conditions (Figure S5D), suggesting that light regulation of adaptive thermogenesis in BAT is ipRGC dependent. Next, we monitored the iBAT surface temperature in OPN4-KO^{SON} mice, in which melanopsin was selectively knocked out in SON-projecting ipRGCs. As expected, in these mice, light no longer blocked BAT-mediated adaptive thermogenesis (Figures 5L–5N), neither did light prevent the upregulation of *Ucp1/Pgc1a/Dio2* in BAT following glucose loading (Figure S5E). Light also did not block BAT-mediated adaptive thermogenesis when there was selective inhibition of neural pathways, namely, SON^{AVP}-PVN, PVN-NTS, and NTS^{Vgat} -RPa (Figures S5F–S5I). These findings collectively indicate that light blocks adaptive thermogenesis in BAT through the retinal ipRGC-SON-PVN-NTS-RPa pathway and thereby decreases GT.

Light modulation of human GT depends on BAT activity

To examine whether light similarly decreases GT in humans, 12 healthy volunteers (subject characteristics, Table S1; STAR Methods) were recruited for a 75-g oral glucose tolerance test

Figure 3. SONAVP-PVN projection mediates light decrease of GT

(A–C) Experiment of monosynaptic tracing (A). Image of rabies virus (RV)- mRuby3 (red) overlapped with melanopsin immunofluorescence (green) in the *Oxt-Cre* (top) and *Avp-Cre* (bottom) retina (B). Quantification of RV^+-ipRGCs (C) in the retina of *Oxt-Cre* mice (72 cells from 2 mice) and in the retina of *Avp-Cre* mice (15 cells from 2 mice). We observed approximately 5-fold more ipRGCs retrogradely labeled from SON^{OXT} than from SON^{AVP}.

(D and E) GT evaluation following CNO-induced inhibition of OXT neurons ([D] n = 9 mice) or AVP neurons ([E] n = 13 mice). Both by two-way ANOVA, Tukey's post hoc test.

(F and G) Experiment of monosynaptic tracing, same as in (A), for evaluating the reciprocal projections between AVP and OXT neurons within SON. In *Oxt-Cre* mice (top), AVP neurons (cyan immunofluorescence) providing monosynaptic input to starter neurons (OXT neurons) are labeled with RV-mRuby3 (red). In *Avp-Cre* mice (bottom), OXT neurons (cyan immunofluorescence) providing monosynaptic input to starter neurons (AVP neurons) are labeled with RV-mRuby3 (red) (F). In (G), the percentage of RV^+-AVP^+ neurons in total AVP^+ neurons (23.1% ± 3.2%, n = 3 mice) and of RV^+-OXT^+ neurons in total OXT^+ neurons (43.8% ± 4.6%, n = 3 mice) are shown for *Oxt-Cre* mice and *Avp-Cre* mice, respectively.

(H–J) Retrograde tracing experiment was used to identify the PVN-projecting SON neuron types (H). Image of immunohistochemistry against AVP neuros (red, top) or OXT neurons (red, bottom) overlapped with PVN-projecting SON neurons (green) (I). Percentage of AVP^+&$EYFP^+$ (75.2% ± 2.5%) or OXT^+&$EYFP^+$ (16.5% ± 5.6%) cells in PVN-projecting SON $EYFP^+$ neurons (J), n = 3 mice/group.

(K) Schematic and image of specifically inhibiting PVN-projecting SON^{AVP} neurons. GT evaluation with CNO-induced inhibition of SON^{AVP}-PVN (n = 9 mice) pathway. Two-way ANOVA, Tukey's post hoc test.

*p < 0.05, **p < 0.01, and ***p < 0.001. Data were represented as mean ± SEM. Scale bars, 25 μm in (B), (F), (I), and (K).

See also Figure S3.

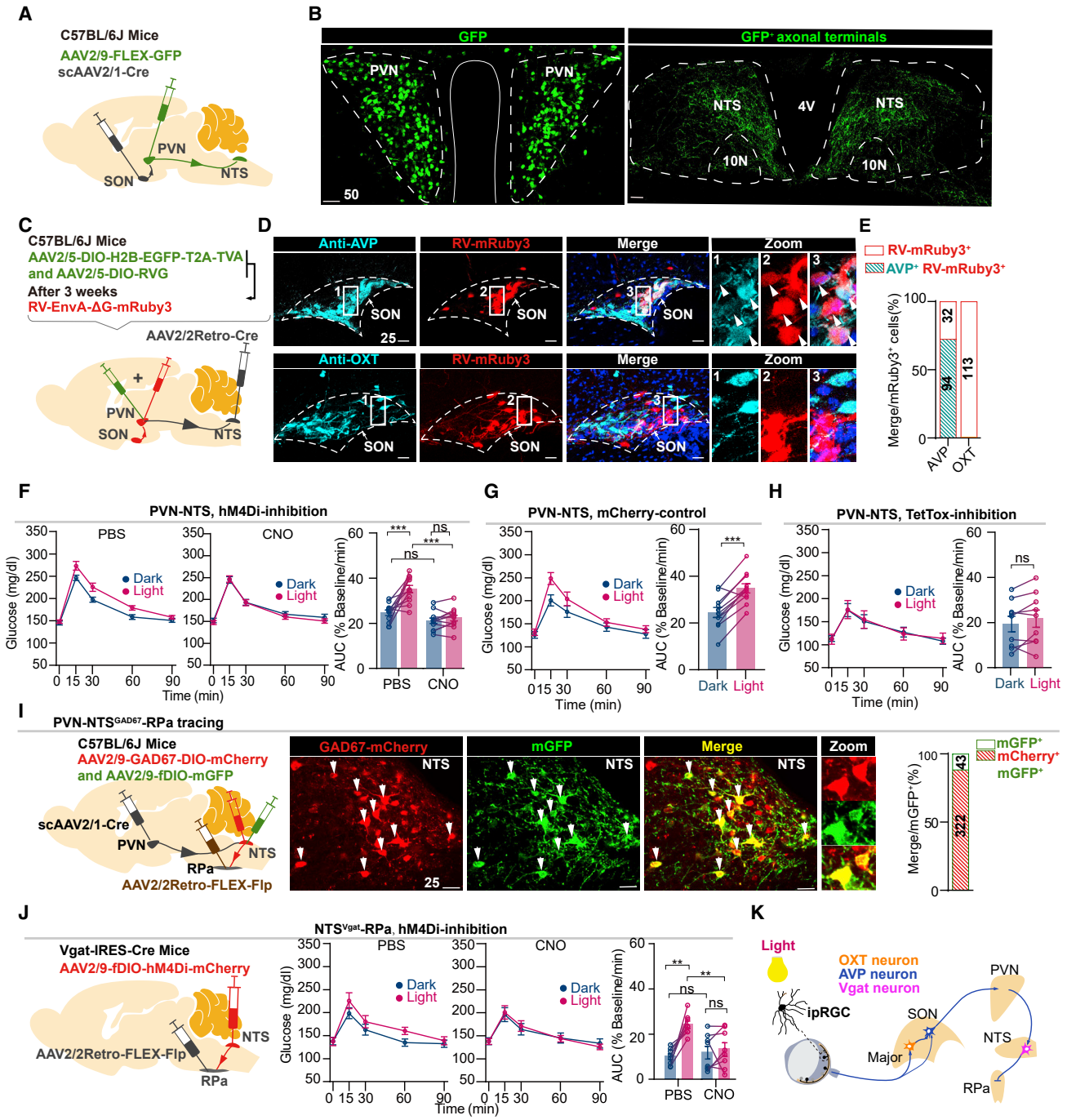

Figure 4. PVN-NTS^{Vgat}-RPa projection mediates light decrease of GT

(A and B) Schematic of the anterograde trans-synaptic tracing (A). Image of SON-innervated PVN neurons and their axonal terminals (B).

(C–E) Schematic of RV-mediated monosynaptic tracing in NTS-projecting PVN neurons (C). Close-up showing co-localization of RV-mRuby3 (red) with immunofluorescence staining of AVP neurons (top, cyan) but not with OXT neurons of SON (bottom, cyan) (D). Percentage of RV$^+$&AVP$^+$ (72.5% ± 2.9%, n = 3 mice) or RV$^+$&OXT$^+$ (0, n = 4 mice) cells in RV$^+$ neurons in SON (E).

(F–H) GT evaluation with CNO-induced ([F] n = 12 mice) and TetTox-mediated ([H] n = 9 mice) inhibition of PVN-NTS pathway (n = 12 mice). GT evaluation in mCherry-mediated control group ([G] control, n = 11 mice). Two-way ANOVA, Tukey's post hoc test for (F). Two-tailed paired t test for both (G) and (H).

(I) The tracing experiment was used to identify the type of neurons of NTS within PVN-NTS-RPa pathway. Close-up showing co-localization (yellow) of GABAergic NTS neurons within PVN-NTS-RPa pathway. Percentage of GABAergic neurons in NTS neurons relaying PVN inputs to RPa (88.4% ± 1.4%, n = 3 mice).

(legend continued on next page)

(OGTT) during daytime (Figure 6A) at an ambient temperature of ~19°C, during which BAT thermogenesis is active.[38] Each subject underwent two sessions, one with the lights on (~400 lux, Figure S6B) and the other in darkness, spaced 3 days apart. These volunteers exhibited a higher AUC (decreased GT) in light (white LED light, Figures 6A and S6A). We also performed OGTT during nighttime (14 healthy volunteers, Table S1). Here, there was also a higher AUC (decreased GT) under light conditions (Figures 6B and S6A), confirming that the effect of light on human GT was independent of circadian phase, which was consistent with what was observed in our mice experiments.

In addition, we evaluated human GT (14 healthy volunteers, Table S1) under blue and red LED light conditions (Figure S6B) and found that blue rather than red light exposure decreased GT (Figures 6C and S6A).

To further evaluate the relevance of BAT thermogenesis in human glucose regulation (10 healthy volunteers, Table S1), the GT assessment was repeated at ~29°C, which is within the human thermoneutral zone (26°C–33°C) where BAT-mediated adaptive thermogenesis is restricted.[38,39] The AUC was no longer affected by the presence or absence of light (white LED light) (Figures 6D and S6A). These data suggest that light indeed decreased human GT and that this likely involved inhibition of BAT-mediated adaptive thermogenesis.

DISCUSSION

Glucose homeostasis is achieved through highly orchestrated processes that detect and respond to fluctuations in internal and external environments. We present evidence that the retina-SON-BAT axis mediates the effect of light on GT. Light decreases GT by activating ipRGCs, leading to inhibition of BAT-mediated adaptive thermogenesis through β3-adrenergic signaling (Figure 6E).

Disruptions of the core circadian clock in the SCN can affect metabolism.[19,40] IpRGC innervation of the SCN influences circadian rhythms.[41,42] Therefore, it is speculated that light may regulate glucometabolism via the SCN. However, in the present study, the SCN excitotoxic lesion, which abolished the circadian rhythm, had no effect on light regulation of GT; whereas the SON lesion prevented light from affecting GT. A previous study reported that SCN lesion alters insulin sensitivity mainly by regulating endogenous glucose production, but not glucose clearance,[43] which is consistent with our observation. More importantly, selective ablation of SON-innervating ipRGCs, but not SCN-innervating ipRGCs, also abolished the effect of light on GT. Taken together, these observations indicate that light acutely modulates GT in a circadian-independent manner involving the SON but not the SCN.

OXT and AVP neurons constitute the majority of SON/PVN neurons in the hypothalamus, besides being components of neural circuits involved in light modulation of glucose metabolism. It is well established that these neurons extend their axons to the pituitary and exert regulatory roles in a neuroendocrine manner by producing and secreting neuropeptides into circulation[44]; these neuropeptides can regulate glucose metabolism in a dose-dependent fashion.[45–47] However, in our study, no difference was detected in the plasma levels of either neuropeptide OXT or AVP between darkness and light conditions. In addition, inhibition of a downstream nucleus, such as NTS, fully prevented light from affecting GT. Therefore, our results suggest that the effect of light on GT requires a direct neural circuit involving SON, instead of neuroendocrine.

It is worth noting that there are several extraocular opsins.[48,49] Whether light reception by these opsins participates in the light-mediated modulation of glucose observed in our study should be considered. However, our experiments with OPN4-KO mice (*Opn4*$^{-/-}$) and *OPN4*$^{f/f}$ mice (OPN4-KO^{SON}) established the requisite role of melanopsin-expressing ipRGCs. Our inhibitory manipulations of the neural circuit further ruled out the possibility that extraocular opsins contribute to the effect of light on glucose metabolism.

BAT is a specialized thermogenic organ with roles in energy metabolism and temperature regulation. Diet-induced thermogenesis (DIT) relies on UCP1 in BAT.[50–53] In this study, light regulation of BAT thermogenesis is also associated with expression of *Ucp1/Pgc1a/Dio2* in BAT after i.p. injection of glucose. It is possible that light might work with DIT to affect BAT energy metabolism, which need further investigation. BAT activity is also regulated by central and peripheral circadian clocks.[54–59] Daily temperature fluctuations have been shown to provide powerful entrainment for peripheral oscillators, including BAT.[60–62] The present study focuses on the acute effect of light/dark exposure (3.5 h) on BAT activity by sympathetic signaling, but it does not evaluate more long-term effects of dark/light exposure on BAT thermogenesis. However, when exposed to aberrant light/dark conditions for a prolonged period, the circuit described here might contribute to the interactions of peripheral circadian clocks and light on BAT activities.

There are daily changes in glucose metabolism at different times of the day/night cycle.[63,64] Higher GT was observed at the active phase (night) compared with the inactive phase (day) in mice (a nocturnal species).[65,66] A similar phenomenon occurs in humans (a diurnal species).[67–71] Our results also showed the effect of the circadian phase on GT in both mice and humans with higher GT at the active phase compared with the inactive phase (for mice, see Figures 1D and S1E; for humans, see Figures 6A and 6B). Importantly, our results from both humans and mice show that light regulation of GT is independent of the circadian phases (Figure 6E). Particularly for humans, GT during nighttime (inactive phase) is worse than that during daytime

(J) Schematic of selective inhibition of RPa-projecting GABAergic neurons in NTS of *Vgat-Cre* mice (NTS^{Vgat}). GT evaluation following inhibition of NTS^{Vgat}-RPa pathway (n = 8 mice). Two-way ANOVA, Tukey's post hoc test.

(K) Model of the light-induced decrease in GT via ipRGCs-SON^{OXT}-SON^{AVP}-PVN-NTS^{Vgat}-RPa pathway.

*p < 0.05, **p < 0.01, and ***p < 0.001. Data were represented as mean ± SEM. Scale bars, 50 μm in (B) and 25 μm in (D) and (I).

See also Figure S4.

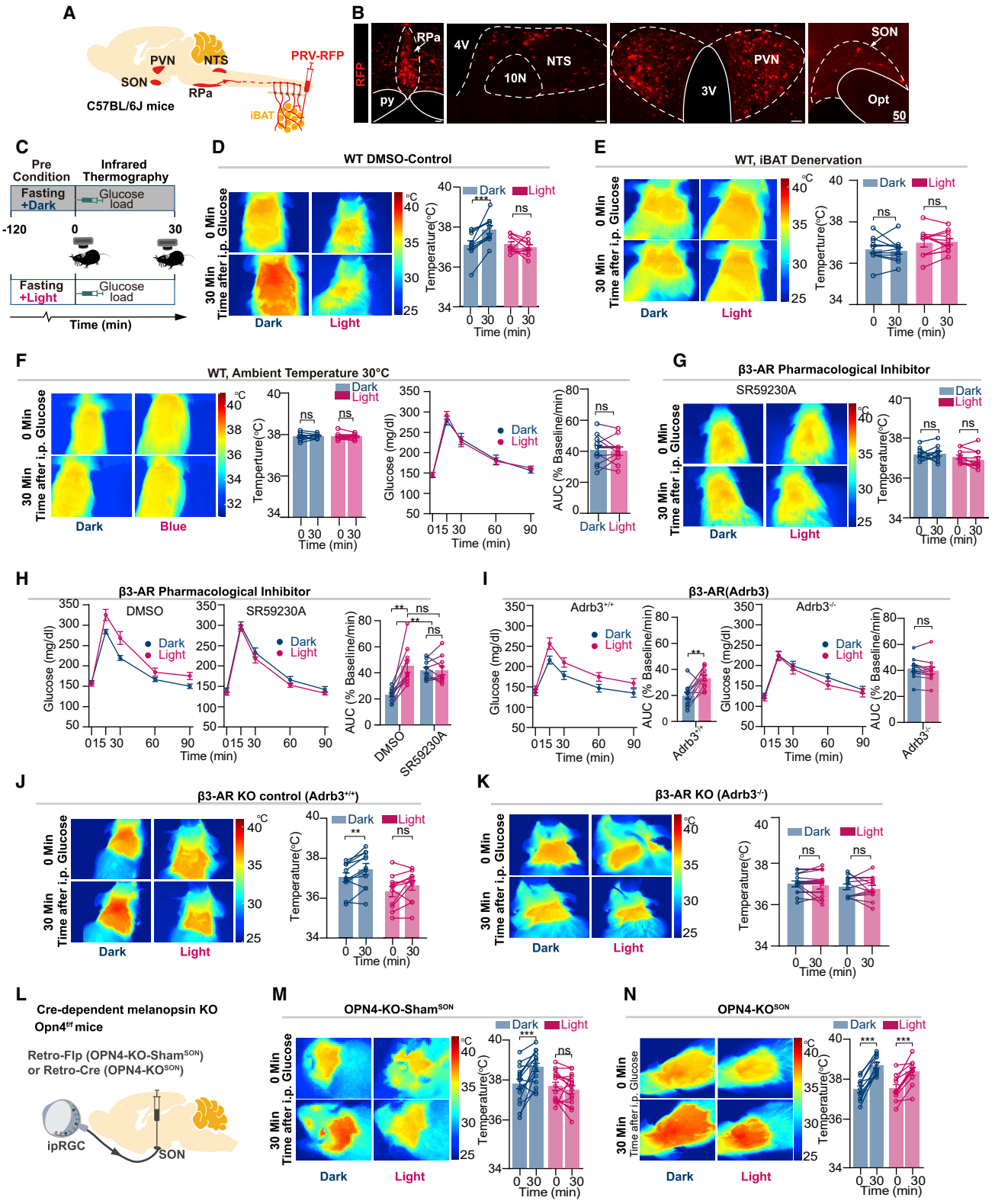

Figure 5. Light decreases GT through blocking BAT-mediated adaptive thermogenesis

(A and B) Experiment of PRV-mediated retrograde polysynaptic tracing (A). Images showing RFP^{+} neurons in RPa, NTS, PVN, and SON (B) that were polysynaptically linked to iBAT.

(legend continued on next page)

(active phase), and on top of this, nighttime light further impairs GT, resulting in an even worsened condition. Therefore, the metabolic impact of nighttime light should be considered, especially when nighttime dining is common among the general population. Providing ambient light at appropriate spectral qualities or intensities may be beneficial for public health.

Endotherms rely on BAT thermogenesis to maintain core body temperature in ever-changing environments.[72] For wild animals, emerging from dens may result in fast and dramatic changes in the level of heat radiation from sunlight. The pathway we describe might provide a means for the fast regulation of thermogenesis in response to altered sun radiation. Interestingly, short-wavelength (blue) light is most effective at activating ipRGCs and thereby repressing BAT thermogenesis according to our model. This acute inhibition of thermogenesis might thus generate a 'cold' feeling. Such engram may be relevant to the hue-heat effect in psychophysics.[73] In the post-industrial era, exposure to excessive artificial lighting seriously perturbs metabolic homeostasis.[13,20] Our findings in mice and humans provide one possible explanation for the epidemiologic observations and may reveal a potential prevention and treatment strategy for metabolic disorders, for instance, by optimizing indoor lighting conditions (intensity and spectrum).

Limitations of the study

This study demonstrates an important role of light itself in regulating glucose metabolism by blocking the BAT-mediated adaptive thermogenesis via the retina-brain-adipose tissue axis. It would be interesting to further investigate the mechanisms underlying light-mediated regulation of other metabolic pathways important for human health, including fat metabolism and amino acid metabolism. Additionally, it is also important to understand the molecular mechanism of how BAT responds to light/dark alteration. Further clinical and animal studies are warranted to determine the long-term effects of light/dark conditions on weight control and the prevention of metabolic disorders.

STAR★METHODS

Detailed methods are provided in the online version of this paper and include the following:

SUPPLEMENTAL INFORMATION

Supplemental information can be found online at https://doi.org/10.1016/j.cell.2022.12.024.

ACKNOWLEDGMENTS

This work was funded by the National Key Basic Research Program of China (grant no. 2020YFA0112200 to T.X.); the CAS priority research program (grant no. XDB39050300 to T.X.); the National Natural Science Foundation of China (grant no. 32121002and 81925009 to T.X., 31900712 and 32271040 to Y.-Q.M., 82201230 to R.L., 61727811 to Huan Zhao, and 81900855 to M.Z.); the CAS Project for Young Scientists in Basic Research (YSBR-013 to T.X. and YSBR-041 to R.L.); the Anhui Provincial Natural Science Foundation (grant no. 2208085J29 to M.Z. and 1908085MC66 to J.-J.M.); the Tencent Foundation through the XPLORER PRIZE to T.X.; the Feng Foundation of Biomedical Research; the Collaborative Innovation Program of Hefei Science Center, CAS (2022HSC-CIP015 to M.Z.); and the National Science and Technology Innovation 2030 Major Program (2021ZD0203100 to Y.-Q.M. and 2022ZD0210000 to R.L.).

(C) Schematic of infrared thermography. iBAT surface temperature was measured at 0 min and at 30 min after glucose loading.
(D) iBAT surface temperature after control (DMSO) treatment in WT mice. n = 10 mice. Two-tailed paired t test.
(E) iBAT surface temperature in WT mice (n = 11) after surgical denervation. Both by two-tailed paired t test.
(F) iBAT thermogenesis and GT evaluation at thermoneutrality in WT mice (n = 10). Both by two-tailed paired t test.
(G) iBAT surface temperature after SR59230A treatment, a selective β3-adrenergic receptor (β3AR) antagonist (1mg/kg intraperitoneally injected 30 min prior to glucose loading). n = 10 mice. Two-tailed paired t test.
(H) GT evaluation after SR59230A or DMSO treatment (n = 10 mice). Two-way ANOVA, Tukey's post hoc test.
(I) GT evaluation in β3AR knockout mice (*Adrb3*$^{-/-}$, n = 12) and littermate controls (*Adrb3*$^{+/+}$, n = 11). Both by two-tailed paired t test.
(J and K) iBAT surface temperature in Adrb3$^{+/+}$ ([J] n = 11) and Adrb3$^{-/-}$ ([K] n = 12) mice. Both by two-tailed paired t test.
(L–N) Schematic of genetically ablating melanopsin (OPN4) in *Opn4*$^{f/f}$ mice (cre-dependent knock out of melanopsin) (L). The iBAT surface temperature in OPN4-KO-Sham^{SON} ([M] n = 15) and OPN4-KO^{SON} ([N] n = 11) mice. Both by two-tailed paired t test.
*p < 0.05, **p < 0.01, and ***p < 0.001. Data were represented as mean ± SEM. Scale bars, 50 μm in (B).
See also Figure S5.

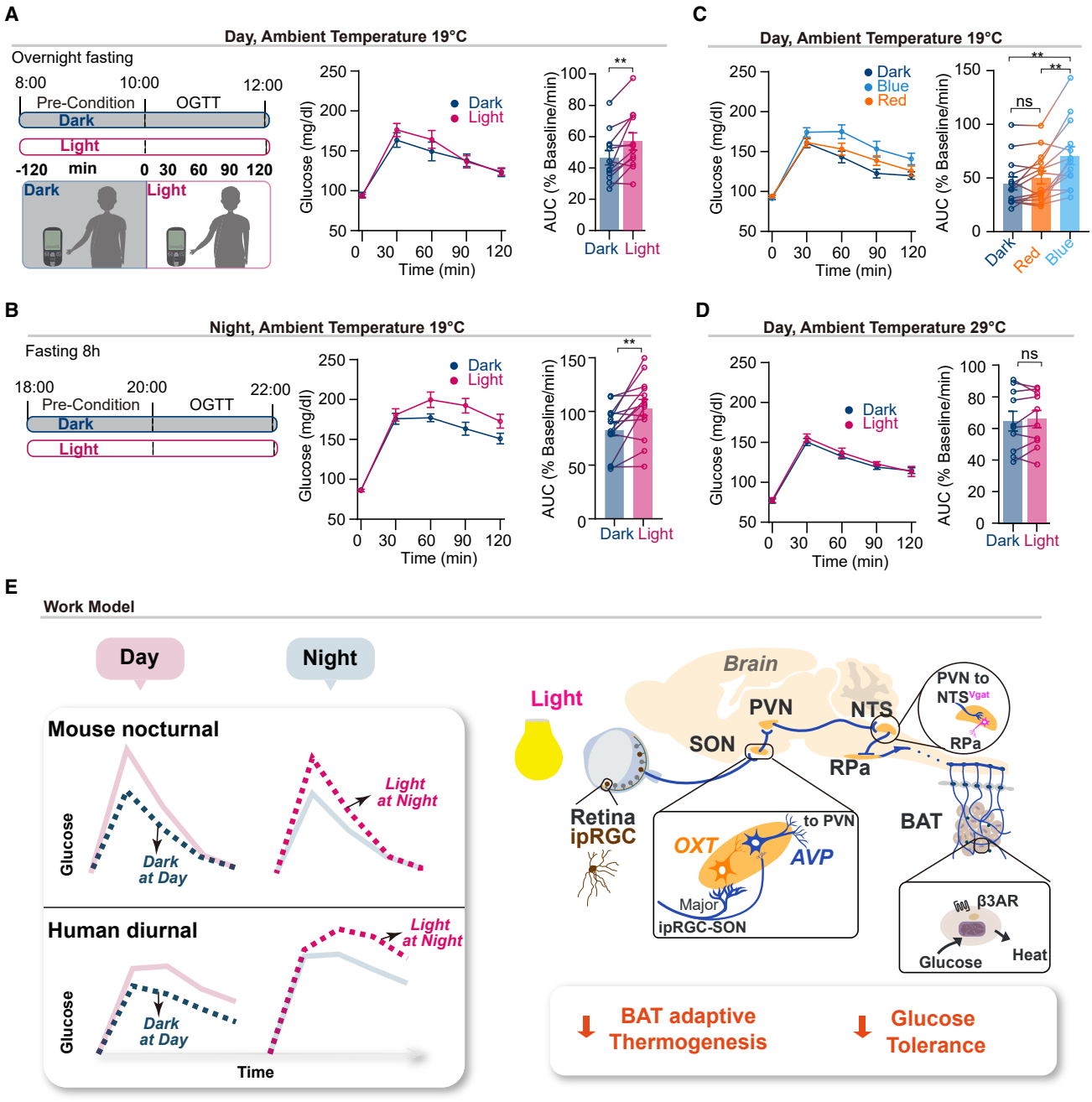

Figure 6. Light decrease of human GT dependent on BAT activity

(A) Schematic of 75-g oral glucose tolerance test (OGTT) for humans during daytime. Volunteers were subjected to OGTT twice with a 3-day interval between the light (400 lux)/dark conditions. GT evaluation during daytime at ~19°C ambient temperature where BAT-mediated adaptive thermogenesis was actived (n = 12). Two-tailed paired t test.

(B) Humans GT evaluation during nighttime. n = 14. By two-tailed paired t test.

(C) Humans GT evaluation under the blue/red light. n = 14. By one-way ANOVA, Tukey's multiple comparisons test.

(D) GT evaluation at ~29°C ambient temperature, within the thermoneutral zone where BAT-mediated adaptive thermogenesis was restricted (n = 10). Two-tailed paired t test.

(E) Work model: light regulation of GT was independent of active/inactive phase in both humans and mice. Light activates intrinsically photosensitive retinal ganglion cells' (ipRGCs) inputs to the oxytocin (OXT) neurons and to vasopressin (AVP) neurons in the supraoptic nucleus (SON), next to the paraventricular nucleus (PVN); to GABAergic neurons in solitary tract nucleus (NTS); to rostral raphe pallidus (RPa); and to the brown adipose tissue (BAT). This circuitry mediates decrease of the BAT thermogenesis through β3-adrenergic signaling and decreases glucose tolerance (GT).

*p < 0.05, **p < 0.01, and ***p < 0.001. Data were represented as mean ± SEM.

See also Figure S6 and Table S1.

AUTHOR CONTRIBUTIONS

Conceptualization, T.X.; methodology, J.-J.M., J.-W.S., and T.X.; validation, T.X.; formal analysis, J.-J.M., J.-W.S., and T.X.; investigation, J.-J.M., J.-W.S., G.L., C.-J.O., J.-X.H., Z.-S.L., Hang Zhao, Y.-M.S., M.Z., R.L., J.-T.C., Y.-Q.M., Huan Zhao, and T.X.; writing, J.-J.M., J.-W.S., G.L., Huan Zhao, and T.X.; supervision, T.X.; funding acquisition, T.X.

DECLARATION OF INTERESTS

The authors declare no competing interests.

Received: March 17, 2022
Revised: September 22, 2022
Accepted: December 13, 2022
Published: January 19, 2023

REFERENCES

1. Berson, D.M., Dunn, F.A., and Takao, M. (2002). Phototransduction by retinal ganglion cells that set the circadian clock. Science *295*, 1070–1073. https://doi.org/10.1126/science.1067262.
2. Lucas, R.J., Hattar, S., Takao, M., Berson, D.M., Foster, R.G., and Yau, K.W. (2003). Diminished pupillary light reflex at high irradiances in melanopsin-knockout mice. Science *299*, 245–247. https://doi.org/10.1126/science.1077293.
3. Chen, S.K., Badea, T.C., and Hattar, S. (2011). Photoentrainment and pupillary light reflex are mediated by distinct populations of ipRGCs. Nature *476*, 92–95. https://doi.org/10.1038/nature10206.
4. Panda, S., Sato, T.K., Castrucci, A.M., Rollag, M.D., DeGrip, W.J., Hogenesch, J.B., Provencio, I., and Kay, S.A. (2002). Melanopsin (Opn4) requirement for normal light-induced circadian phase shifting. Science *298*, 2213–2216. https://doi.org/10.1126/science.1076848.
5. Zhang, Z., Beier, C., Weil, T., and Hattar, S. (2021). The retinal ipRGC-preoptic circuit mediates the acute effect of light on sleep. Nat. Commun. *12*, 5115. https://doi.org/10.1038/s41467-021-25378-w.
6. Lupi, D., Oster, H., Thompson, S., and Foster, R.G. (2008). The acute light-induction of sleep is mediated by OPN4-based photoreception. Nat. Neurosci. *11*, 1068–1073. https://doi.org/10.1038/nn.2179.
7. An, K., Zhao, H., Miao, Y., Xu, Q., Li, Y.F., Ma, Y.Q., Shi, Y.M., Shen, J.W., Meng, J.J., Yao, Y.G., et al. (2020). A circadian rhythm-gated subcortical pathway for nighttime-light-induced depressive-like behaviors in mice. Nat. Neurosci. *23*, 869–880. https://doi.org/10.1038/s41593-020-0640-8.
8. Fernandez, D.C., Fogerson, P.M., Lazzerini Ospri, L., Thomsen, M.B., Layne, R.M., Severin, D., Zhan, J., Singer, J.H., Kirkwood, A., Zhao, H., et al. (2018). Light affects mood and learning through distinct retina-brain pathways. Cell *175*, 71–84.e18. https://doi.org/10.1016/j.cell.2018.08.004.
9. Huang, X., Huang, P., Huang, L., Hu, Z., Liu, X., Shen, J., Xi, Y., Yang, Y., Fu, Y., Tao, Q., et al. (2021). A visual circuit related to the nucleus reuniens for the spatial-memory-promoting effects of light treatment. Neuron *109*, 347–362.e7. https://doi.org/10.1016/j.neuron.2020.10.023.
10. Lam, C.K., Chari, M., and Lam, T.K. (2009). CNS regulation of glucose homeostasis. Physiology (Bethesda) *24*, 159–170. https://doi.org/10.1152/physiol.00003.2009.
11. Tups, A., Benzler, J., Sergi, D., Ladyman, S.R., and Williams, L.M. (2017). Central regulation of glucose homeostasis. Compr. Physiol. *7*, 741–764. https://doi.org/10.1002/cphy.c160015.
12. Obayashi, K., Saeki, K., and Kurumatani, N. (2016). Ambient light exposure and changes in obesity parameters: A longitudinal study of the HEIJO-KYO cohort. J. Clin. Endocrinol. Metab. *101*, 3539–3547. https://doi.org/10.1210/jc.2015-4123.
13. Park, Y.M., White, A.J., Jackson, C.L., Weinberg, C.R., and Sandler, D.P. (2019). Association of exposure to artificial light at night while sleeping with risk of obesity in women. JAMA Intern. Med. *179*, 1061–1071. https://doi.org/10.1001/jamainternmed.2019.0571.
14. Reinke, H., and Asher, G. (2019). Crosstalk between metabolism and circadian clocks. Nat. Rev. Mol. Cell Biol. *20*, 227–241. https://doi.org/10.1038/s41580-018-0096-9.
15. Stenvers, D.J., Scheer, F.A.J., Schrauwen, P., la Fleur, S.E., and Kalsbeek, A. (2019). Circadian clocks and insulin resistance. Nat. Rev. Endocrinol. *15*, 75–89. https://doi.org/10.1038/s41574-018-0122-1.
16. Fonken, L.K., Workman, J.L., Walton, J.C., Weil, Z.M., Morris, J.S., Haim, A., and Nelson, R.J. (2010). Light at night increases body mass by shifting the time of food intake. Proc. Natl. Acad. Sci. USA *107*, 18664–18669. https://doi.org/10.1073/pnas.1008734107.
17. Bedrosian, T.A., Galan, A., Vaughn, C.A., Weil, Z.M., and Nelson, R.J. (2013). Light at night alters daily patterns of cortisol and clock proteins in female Siberian hamsters. J. Neuroendocrinol. *25*, 590–596. https://doi.org/10.1111/jne.12036.
18. Scheer, F.A., Hilton, M.F., Mantzoros, C.S., and Shea, S.A. (2009). Adverse metabolic and cardiovascular consequences of circadian misalignment. Proc. Natl. Acad. Sci. USA *106*, 4453–4458. https://doi.org/10.1073/pnas.0808180106.
19. Fonken, L.K., and Nelson, R.J. (2014). The effects of light at night on circadian clocks and metabolism. Endocr. Rev. *35*, 648–670. https://doi.org/10.1210/er.2013-1051.
20. Russart, K.L.G., and Nelson, R.J. (2018). Light at night as an environmental endocrine disruptor. Physiol. Behav. *190*, 82–89. https://doi.org/10.1016/j.physbeh.2017.08.029.
21. Fan, X., Chen, D., Wang, Y., Tan, Y., Zhao, H., Zeng, J., Li, Y., Guo, X., Qiu, H., and Gu, Y. (2022). Light intensity alters the effects of light-induced circadian disruption on glucose and lipid metabolism in mice. Am. J. Physiol. Endocrinol. Metab. *322*, E1–E9. https://doi.org/10.1152/ajpendo.00025.2021.
22. Govardovskii, V.I., Fyhrquist, N., Reuter, T., Kuzmin, D.G., and Donner, K. (2000). In search of the visual pigment template. Vis. Neurosci. *17*, 509–528. https://doi.org/10.1017/s0952523800174036.
23. Xue, T., Do, M.T., Riccio, A., Jiang, Z., Hsieh, J., Wang, H.C., Merbs, S.L., Welsbie, D.S., Yoshioka, T., Weissgerber, P., et al. (2011). Melanopsin signalling in mammalian iris and retina. Nature *479*, 67–73. https://doi.org/10.1038/nature10567.
24. Hattar, S., Kumar, M., Park, A., Tong, P., Tung, J., Yau, K.W., and Berson, D.M. (2006). Central projections of melanopsin-expressing retinal ganglion cells in the mouse. J. Comp. Neurol. *497*, 326–349. https://doi.org/10.1002/cne.20970.
25. Dietrich, M.O., and Horvath, T.L. (2013). Hypothalamic control of energy balance: insights into the role of synaptic plasticity. Trends Neurosci. *36*, 65–73. https://doi.org/10.1016/j.tins.2012.12.005.
26. Wang, Q., Yue, W.W.S., Jiang, Z., Xue, T., Kang, S.H., Bergles, D.E., Mikoshiba, K., Offermanns, S., and Yau, K.W. (2017). Synergistic signaling by light and acetylcholine in mouse iris sphincter muscle. Curr. Biol. *27*, 1791–1800.e5. https://doi.org/10.1016/j.cub.2017.05.022.
27. Nakamura, K., Velho, G., and Bouby, N. (2017). Vasopressin and metabolic disorders: translation from experimental models to clinical use. J. Intern. Med. *282*, 298–309. https://doi.org/10.1111/joim.12649.
28. Lawson, E.A., Olszewski, P.K., Weller, A., and Blevins, J.E. (2020). The role of oxytocin in regulation of appetitive behaviour, body weight and glucose homeostasis. J. Neuroendocrinol. *32*, e12805. https://doi.org/10.1111/jne.12805.
29. Luo, F., Mu, Y., Gao, C., Xiao, Y., Zhou, Q., Yang, Y., Ni, X., Shen, W.L., and Yang, J. (2019). Whole-brain patterns of the presynaptic inputs and axonal projections of BDNF neurons in the paraventricular nucleus. J. Genet. Genomics *46*, 31–40. https://doi.org/10.1016/j.jgg.2018.11.004.
30. Wang, P., Loh, K.H., Wu, M., Morgan, D.A., Schneeberger, M., Yu, X., Chi, J., Kosse, C., Kim, D., Rahmouni, K., et al. (2020). A leptin-BDNF pathway

regulating sympathetic innervation of adipose tissue. Nature *583*, 839–844. https://doi.org/10.1038/s41586-020-2527-y.

31. An, J.J., Liao, G.Y., Kinney, C.E., Sahibzada, N., and Xu, B. (2015). Discrete BDNF neurons in the paraventricular hypothalamus control feeding and energy expenditure. Cell Metab. *22*, 175–188. https://doi.org/10.1016/j.cmet.2015.05.008.

32. Kenney, M.J., Weiss, M.L., and Haywood, J.R. (2003). The paraventricular nucleus: an important component of the central neurocircuitry regulating sympathetic nerve outflow. Acta Physiol. Scand. *177*, 7–15. https://doi.org/10.1046/j.1365-201X.2003.01042.x.

33. Cao, W.H., Madden, C.J., and Morrison, S.F. (2010). Inhibition of brown adipose tissue thermogenesis by neurons in the ventrolateral medulla and in the nucleus tractus solitarius. Am. J. Physiol. Regul. Integr. Comp. Physiol. *299*, R277–R290. https://doi.org/10.1152/ajpregu.00039.2010.

34. Keinan, O., Valentine, J.M., Xiao, H., Mahata, S.K., Reilly, S.M., Abu-Odeh, M., Deluca, J.H., Dadpey, B., Cho, L., Pan, A., et al. (2021). Glycogen metabolism links glucose homeostasis to thermogenesis in adipocytes. Nature *599*, 296–301. https://doi.org/10.1038/s41586-021-04019-8.

35. Hankir, M.K., Cowley, M.A., and Fenske, W.K. (2016). A BAT-centric approach to the treatment of diabetes: turn on the brain. Cell Metab. *24*, 31–40. https://doi.org/10.1016/j.cmet.2016.05.003.

36. Vaughan, C.H., Zarebidaki, E., Ehlen, J.C., and Bartness, T.J. (2014). Analysis and measurement of the sympathetic and sensory innervation of white and brown adipose tissue. Methods Enzymol. *537*, 199–225. https://doi.org/10.1016/B978-0-12-411619-1.00011-2.

37. Morgan, D.A., McDaniel, L.N., Yin, T., Khan, M., Jiang, J., Acevedo, M.R., Walsh, S.A., Ponto, L.L., Norris, A.W., Lutter, M., et al. (2015). Regulation of glucose tolerance and sympathetic activity by MC4R signaling in the lateral hypothalamus. Diabetes *64*, 1976–1987. https://doi.org/10.2337/db14-1257.

38. Pallubinsky, H., Schellen, L., and van Marken Lichtenbelt, W.D. (2019). Exploring the human thermoneutral zone - A dynamic approach. J. Therm. Biol. *79*, 199–208. https://doi.org/10.1016/j.jtherbio.2018.12.014.

39. Cannon, B., and Nedergaard, J. (2011). Nonshivering thermogenesis and its adequate measurement in metabolic studies. J. Exp. Biol. *214*, 242–253. https://doi.org/10.1242/jeb.050989.

40. Mason, I.C., Qian, J., Adler, G.K., and Scheer, F.A.J. (2020). Impact of circadian disruption on glucose metabolism: implications for type 2 diabetes. Diabetologia *63*, 462–472. https://doi.org/10.1007/s00125-019-05059-6.

41. Fonken, L.K., Aubrecht, T.G., Meléndez-Fernández, O.H., Weil, Z.M., and Nelson, R.J. (2013). Dim light at night disrupts molecular circadian rhythms and increases body weight. J. Biol. Rhythms *28*, 262–271. https://doi.org/10.1177/0748730413493862.

42. LeGates, T.A., Fernandez, D.C., and Hattar, S. (2014). Light as a central modulator of circadian rhythms, sleep and affect. Nat. Rev. Neurosci. *15*, 443–454. https://doi.org/10.1038/nrn3743.

43. Coomans, C.P., van den Berg, S.A., Lucassen, E.A., Houben, T., Pronk, A.C., van der Spek, R.D., Kalsbeek, A., Biermasz, N.R., Willems van Dijk, K., Romijn, J.A., and Meijer, J.H. (2013). The suprachiasmatic nucleus controls circadian energy metabolism and hepatic insulin sensitivity. Diabetes *62*, 1102–1108. https://doi.org/10.2337/db12-0507.

44. Romanov, R.A., Alpár, A., Hökfelt, T., and Harkany, T. (2019). Unified classification of molecular, network, and endocrine features of hypothalamic neurons. Annu. Rev. Neurosci. *42*, 1–26. https://doi.org/10.1146/annurev-neuro-070918-050414.

45. Aoyagi, T., Birumachi, J., Hiroyama, M., Fujiwara, Y., Sanbe, A., Yamauchi, J., and Tanoue, A. (2007). Alteration of glucose homeostasis in V1a vasopressin receptor-deficient mice. Endocrinology *148*, 2075–2084. https://doi.org/10.1210/en.2006-1315.

46. Snider, B., Geiser, A., Yu, X.P., Beebe, E.C., Willency, J.A., Qing, K., Guo, L., Lu, J., Wang, X., Yang, Q., et al. (2019). Long-acting and selective oxytocin peptide analogs show antidiabetic and antiobesity effects in male mice. J. Endocr. Soc. *3*, 1423–1444. https://doi.org/10.1210/js.2019-00004.

47. Taveau, C., Chollet, C., Bichet, D.G., Velho, G., Guillon, G., Corbani, M., Roussel, R., Bankir, L., Melander, O., and Bouby, N. (2017). Acute and chronic hyperglycemic effects of vasopressin in normal rats: involvement of V1A receptors. Am. J. Physiol. Endocrinol. Metab. *312*, E127–E135. https://doi.org/10.1152/ajpendo.00269.2016.

48. Zhang, K.X., D'Souza, S., Upton, B.A., Kernodle, S., Vemaraju, S., Nayak, G., Gaitonde, K.D., Holt, A.L., Linne, C.D., Smith, A.N., et al. (2020). Violet-light suppression of thermogenesis by opsin 5 hypothalamic neurons. Nature *585*, 420–425. https://doi.org/10.1038/s41586-020-2683-0.

49. Nayak, G., Zhang, K.X., Vemaraju, S., Odaka, Y., Buhr, E.D., Holt-Jones, A., Kernodle, S., Smith, A.N., Upton, B.A., D'Souza, S., et al. (2020). Adaptive thermogenesis in mice is enhanced by opsin 3-dependent adipocyte light sensing. Cell Rep. *30*, 672–686.e8. https://doi.org/10.1016/j.celrep.2019.12.043.

50. Li, Y., Schnabl, K., Gabler, S.M., Willershäuser, M., Reber, J., Karlas, A., Laurila, S., Lahesmaa, M., Din, M.U., Bast-Habersbrunner, A., et al. (2018). Secretin-activated brown fat mediates prandial thermogenesis to induce satiation. Cell *175*. 1561-1574.e1512. https://doi.org/10.1016/j.cell.2018.10.016.

51. Lin, J., Jiang, X., Dong, M., Liu, X., Shen, Q., Huang, Y., Zhang, H., Ye, R., Zhou, H., Yan, C., et al. (2021). Hepatokine pregnancy zone protein governs the diet-induced thermogenesis through activating brown adipose tissue. Adv. Sci. (Weinh) *8*, e2101991. https://doi.org/10.1002/advs.202101991.

52. von Essen, G., Lindsund, E., Cannon, B., and Nedergaard, J. (2017). Adaptive facultative diet-induced thermogenesis in wild-type but not in UCP1-ablated mice. Am. J. Physiol. Endocrinol. Metab. *313*, E515–E527. https://doi.org/10.1152/ajpendo.00097.2017.

53. Nedergaard, J., and Cannon, B. (2022). Diet-induced thermogenesis: principles and pitfalls. Methods Mol. Biol. *2448*, 177–202. https://doi.org/10.1007/978-1-0716-2087-8_12.

54. Straat, M.E., Hogenboom, R., Boon, M.R., Rensen, P.C.N., and Kooijman, S. (2021). Circadian control of brown adipose tissue. Biochim. Biophys. Acta Mol. Cell Biol. Lipids *1866*, 158961. https://doi.org/10.1016/j.bbalip.2021.158961.

55. van den Berg, R., Kooijman, S., Noordam, R., Ramkisoensing, A., Abreu-Vieira, G., Tambyrajah, L.L., Dijk, W., Ruppert, P., Mol, I.M., Kramar, B., et al. (2018). A diurnal rhythm in brown adipose tissue causes rapid clearance and combustion of plasma lipids at wakening. Cell Rep. *22*, 3521–3533. https://doi.org/10.1016/j.celrep.2018.03.004.

56. Gerhart-Hines, Z., and Lazar, M.A. (2015). Circadian metabolism in the light of evolution. Endocr. Rev. *36*, 289–304. https://doi.org/10.1210/er.2015-1007.

57. Chappuis, S., Ripperger, J.A., Schnell, A., Rando, G., Jud, C., Wahli, W., and Albrecht, U. (2013). Role of the circadian clock gene Per2 in adaptation to cold temperature. Mol. Metab. *2*, 184–193. https://doi.org/10.1016/j.molmet.2013.05.002.

58. Gerhart-Hines, Z., Feng, D., Emmett, M.J., Everett, L.J., Loro, E., Briggs, E.R., Bugge, A., Hou, C., Ferrara, C., Seale, P., et al. (2013). The nuclear receptor Rev-erbα controls circadian thermogenic plasticity. Nature *503*, 410–413. https://doi.org/10.1038/nature12642.

59. Nam, D., Guo, B., Chatterjee, S., Chen, M.H., Nelson, D., Yechoor, V.K., and Ma, K. (2015). The adipocyte clock controls brown adipogenesis through the TGF-β and BMP signaling pathways. J. Cell Sci. *128*, 1835–1847. https://doi.org/10.1242/jcs.167643.

60. Buhr, E.D., Yoo, S.H., and Takahashi, J.S. (2010). Temperature as a universal resetting cue for mammalian circadian oscillators. Science *330*, 379–385. https://doi.org/10.1126/science.1195262.

61. Adlanmerini, M., Carpenter, B.J., Remsberg, J.R., Aubert, Y., Peed, L.C., Richter, H.J., and Lazar, M.A. (2019). Circadian lipid synthesis in brown fat maintains murine body temperature during chronic cold. Proc. Natl. Acad. Sci. USA *116*, 18691–18699. https://doi.org/10.1073/pnas.1909883116.

62. Kooijman, S., van den Heuvel, J.K., and Rensen, P.C.N. (2015). Neuronal control of brown fat activity. Trends Endocrinol. Metab. *26*, 657–668. https://doi.org/10.1016/j.tem.2015.09.008.

63. Kalsbeek, A., la Fleur, S., and Fliers, E. (2014). Circadian control of glucose metabolism. Mol. Metab. *3*, 372–383. https://doi.org/10.1016/j.molmet.2014.03.002.

64. Qian, J., and Scheer, F.A.J. (2016). Circadian system and glucose metabolism: implications for physiology and disease. Trends Endocrinol. Metab. *27*, 282–293. https://doi.org/10.1016/j.tem.2016.03.005.

65. la Fleur, S.E., Kalsbeek, A., Wortel, J., Fekkes, M.L., and Buijs, R.M. (2001). A daily rhythm in glucose tolerance: a role for the suprachiasmatic nucleus. Diabetes *50*, 1237–1243. https://doi.org/10.2337/diabetes.50.6.1237.

66. Ding, G., Li, X., Hou, X., Zhou, W., Gong, Y., Liu, F., He, Y., Song, J., Wang, J., Basil, P., et al. (2021). REV-ERB in GABAergic neurons controls diurnal hepatic insulin sensitivity. Nature *592*, 763–767. https://doi.org/10.1038/s41586-021-03358-w.

67. Carroll, K.F., and Nestel, P.J. (1973). Diurnal variation in glucose tolerance and in insulin secretion in man. Diabetes *22*, 333–348. https://doi.org/10.2337/diab.22.5.333.

68. Takahashi, M., Ozaki, M., Kang, M.I., Sasaki, H., Fukazawa, M., Iwakami, T., Lim, P.J., Kim, H.K., Aoyama, S., and Shibata, S. (2018). Effects of meal timing on postprandial glucose metabolism and blood metabolites in healthy adults. Nutrients *10*, 1763. https://doi.org/10.3390/nu10111763.

69. Morris, C.J., Yang, J.N., Garcia, J.I., Myers, S., Bozzi, I., Wang, W., Buxton, O.M., Shea, S.A., and Scheer, F.A. (2015). Endogenous circadian system and circadian misalignment impact glucose tolerance via separate mechanisms in humans. Proc. Natl. Acad. Sci. USA *112*, E2225–E2234. https://doi.org/10.1073/pnas.1418955112.

70. Bandín, C., Scheer, F.A., Luque, A.J., Ávila-Gandía, V., Zamora, S., Madrid, J.A., Gómez-Abellán, P., and Garaulet, M. (2015). Meal timing affects glucose tolerance, substrate oxidation and circadian-related variables: A randomized, crossover trial. Int. J. Obes. (Lond.) *39*, 828–833. https://doi.org/10.1038/ijo.2014.182.

71. Sonnier, T., Rood, J., Gimble, J.M., and Peterson, C.M. (2014). Glycemic control is impaired in the evening in prediabetes through multiple diurnal rhythms. J. Diabetes Complications *28*, 836–843. https://doi.org/10.1016/j.jdiacomp.2014.04.001.

72. Cannon, B., and Nedergaard, J. (2004). Brown adipose tissue: function and physiological significance. Physiol. Rev. *84*, 277–359. https://doi.org/10.1152/physrev.00015.2003.

73. Mogensen, M.F., and English, H.B. (1926). The apparent warmth of colors. Am. J. Psychol. *37*, 427–428. https://doi.org/10.2307/1413633.

74. Chen, X., and Li, H. (2017). ArControl: an Arduino-based comprehensive behavioral platform with real-time performance. Front. Behav. Neurosci. *11*, 244.

STAR★METHODS

KEY RESOURCES TABLE

REAGENT or RESOURCE	SOURCE	IDENTIFIER
Antibodies		
Rabbit anti-oxytocin	Abcam	Cat#ab212193; RRID: AB_2895534
Rabbit anti-vasopressin	Immunostar	Cat#20069; RRID: AB_572219
Rabbit anti-melanopsin	Advanced Targeting System	Cat#AB-N38; RRID: AB_1266797
Rabbit anti-GFAP	Sangon Biotech	Cat#D120691
Rabbit anti-cFos	Synaptic Systems	Cat#226003; RRID: AB_2231974
Mouse anti-BDNF	Proteintech	Cat#66292-1-Ig; RRID: AB_2881675
Alexa Fluor™ 488 donkey anti-mouse IgG	Thermo Fisher	Cat#A10680; RRID: AB_2534062
Alexa Fluor™ 488 goat anti-rabbit IgG	Thermo Fisher	Cat#A11034;RRID: AB_2576217
Alexa Fluor™ 568 goat anti-rabbit IgG	Thermo Fisher	Cat#A11036; RRID: AB_10563566
Bacterial and virus strains		
AAV2/2-hEF1α-DIO-ChR2-eYFP	Shanghai Taitool Bioscience Co.Ltd.	Cat#S0199-2
scAAV2/1-hSyn-Cre-pA	Shanghai Taitool Bioscience Co.Ltd.	Cat#S0292-1
AAV2/2Retro-hSyn-Cre	Shanghai Taitool Bioscience Co.Ltd.	Cat#S0278-2R
AAV2/2Retro-hSyn-Flp	Shanghai Taitool Bioscience Co.Ltd.	Cat#S0271-2R
AAV2/2Retro-CAG-FLEX-Flpo	Shanghai Taitool Bioscience Co.Ltd.	Cat#S0273-2R
AAV2/9-hEF1a-DIO-EYFP	Shanghai Taitool Bioscience Co.Ltd.	Cat#S0196-9
AAV2/9-hEF1a-fDIO-mGFP	Shanghai Taitool Bioscience Co.Ltd.	Cat#S0289-9
AAV2/9-hSyn-DIO-hM4Di-mCherry	Shanghai Taitool Bioscience Co.Ltd.	Cat#S0193-9
AAV2/9-hSyn-DIO-mCherry	Shanghai Taitool Bioscience Co.Ltd.	Cat#S0240-9
AAV2/9-hEF1a-fDIO-hM4D(Gi)-mCherry	Shanghai Taitool Bioscience Co.Ltd.	Cat#S0336-9
AAV2/2-hSyn-DIO-hM3Dq-mCherry	Shanghai Taitool Bioscience Co.Ltd.	Cat#S0192-2
AAV2/2-hSyn-DIO-hM4Di-mCherry	Shanghai Taitool Bioscience Co.Ltd.	Cat#S0193-2
AAV2/2-hSyn-DIO-mCherry	Shanghai Taitool Bioscience Co.Ltd.	Cat#S0240-2
AAV2/9-CAG-DIO-EGFP-2A-TetTox	Shanghai Taitool Bioscience Co.Ltd.	Cat#S0235-9
AAV2/5-hEF1a-DIO-RVG	Shanghai Taitool Bioscience Co.Ltd.	Cat#S0325-5
AAV2/5-hEF1a-DIO-H2B-EGFP-T2A-TVA	Shanghai Taitool Bioscience Co.Ltd.	Cat#S0320-5
RV-EnvA-△G-mRuby3	Shanghai Taitool Bioscience Co.Ltd.	Cat#R002
AAV2/9-CAG-FLEX-GFP	OBiO Technology(Shanghai)	Cat#AG28304
AAV2/9-GAD67-DIO-mCherry	OBiO Technology(Shanghai)	Cat#H15084
PRV-CAG-RFP	Brain TVA (Wuhan, China) Co.Ltd.	Cat#P03002
AAV2/2Retro-hEF1a-DIO-ChETA-EYFP	prepared in the Xue laboratory	N/A
Chemicals, peptides, and recombinant proteins		
Ethanol	Sangon Biotech	Cat#A500737
Sucrose	Sangon Biotech	Cat#A100335
DEPC water	Sangon Biotech	Cat#B501005
Triton X-100	Sangon Biotech	Cat#A110694
Bovine albumin	Sangon Biotech	Cat#A600332
Isopropyl alcohol	Sangon Biotech	Cat#A600918
Paraformaldehyde	Sigma-Aldrich	Cat#V900894
Clozapine N-oxide	Sigma-Aldrich	Cat#34233-69-7
N-Methyl-D-aspartic acid	Sigma-Aldrich	Cat#6384-92-5
Sodium carboxymethyl cellulose	Sigma-Aldrich	Cat#9004-32-4
Atopin	Aladdin	Cat#A109524

(*Continued on next page*)

Continued

REAGENT or RESOURCE	SOURCE	IDENTIFIER
(R)-(-)-Phenylephrine Hydrochloride	Aladdin	Cat#G1316011
Chloroform	Sinopharm	Cat#10006818
SYBR Green	Roche	Cat#4913914001
TRIzol Reagent	Thermo Fisher	Cat#15596026
2 × Taq Master Mix (Dye Plus)	Vazyme	Cat#P112-03
Optimal Cutting temperature (O.C.T) Compound	Sakura	Cat#4583
Isoflurane	RWD Life Science Co.,Ltd.	Cat#R510-22-10
Critical commercial assays		
Insulin ELISA kit	Millipore	Cat#EZRMI-13K
Cholecystokinin ELISA kit	Cloud-Clone	Cat#CEA802Mu
Ghrelin ELISA Kit	Elabscience Biotechnology Co.,Ltd.	Cat#E-EL-M0551c
Orexin A ELISA Kit	Elabscience Biotechnology Co.,Ltd.	Cat#E-EL-M0860c
Glucagon ELISA Kit	Elabscience Biotechnology Co.,Ltd.	Cat#E-EL-M0555c
Epinephrine ELISA kit	Elabscience Biotechnology Co.,Ltd.	Cat#E-EL-0045c
Corticosterone ELISA Kit	Elabscience Biotechnology Co.,Ltd.	Cat#E-EL-0161c
Norepinephrine ELISA Kit	Elabscience Biotechnology Co.,Ltd.	Cat#E-EL-0047c
Glucagon Like Peptide 1 ELISA Kit	Elabscience Biotechnology Co.,Ltd.	Cat#E-EL-M3012
Lactate colorimetric kits	Elabscience Biotechnology Co.,Ltd.	Cat#E-BC-K044-M
Growth Hormone colorimetric kits	Elabscience Biotechnology Co.,Ltd.	Cat#E-EL-M0060c
Nonesterified fatty acids colorimetric kits	Elabscience Biotechnology Co.,Ltd.	Cat#E-BC-K013-S
AG Evo M-MLV RT kit	Accurate Biology	Cat#AG11705
Vasopressin radioimmunoassay kit	DIAsource ImmunoAssays S.A.	Cat#KIPERB319
Deposited data		
Blood glucose and iBAT thermogenesis raw data	Mendeley Data	https://doi.org/10.17632/y8nwvjh5pp.1
Experimental models: Organisms/strains		
Mouse: *Opn4*$^{-/-}$	Gift from King-Wai Yau in Johns Hopkins University	N/A
Mouse: *Opn4*^{cre}	Gift from King-Wai Yau in Johns Hopkins University	N/A
Mouse: *Opn4* $^{f/f}$	Gift from King-Wai Yau in Johns Hopkins University	N/A
Mouse: *Cnga3*$^{-/-}$::*Gnat1*$^{-/-}$::*Opn4*$^{+/+}$	Gift from King-Wai Yau in Johns Hopkins University	N/A
Mouse: *Adrb3*$^{-/-}$	Gift from Wen-wen Zeng in Tsinghua University	N/A
Mouse: C57BL/6J	SPF (Beijing) Biotechnology Co., Ltd.	N/A
Mouse: *Oxt-IRES-cre*	Jackson Laboratory	JAX: 024234
Mouse: *Avp-IRES2-cre*	Jackson Laboratory	JAX: 023530
Mouse: *Vgat-IRES-cre*	Jackson Laboratory	JAX: 028862
Mouse: *Ai3*	Jackson Laboratory	JAX: 007903
Oligonucleotides		
Real-time PCR primers	This paper	Methods_Molecular profiling of iBAT tissue
Gapdh-F: 5'-CTGCCCAGAACATCATCCCT-3'	Tsingke Biotechnology Co., Ltd.	N/A
Gapdh-R: 5'-TGAAGTCGCAGGAGACAACC-3'	Tsingke Biotechnology Co., Ltd.	N/A
Ucp1-F: 5'-AAGCTGTGCGATGTCCATGT-3'	Tsingke Biotechnology Co., Ltd.	N/A
Ucp1-R: 5'-AAGCCACAAACCCTTTGAAAA-3'	Tsingke Biotechnology Co., Ltd.	N/A
Pgcla2-F: 5'-AGCCGTGACCACTGACAACGAG-3'	Tsingke Biotechnology Co., Ltd.	N/A
Pgcla2-R: 5'-GCTGCATGGTTCTGAGTGCTAAG-3'	Tsingke Biotechnology Co., Ltd.	N/A

(*Continued on next page*)

Continued

REAGENT or RESOURCE	SOURCE	IDENTIFIER
Dio2-F: 5'-GTCCGCAAATGACCCCTTT-3'	Tsingke Biotechnology Co., Ltd.	N/A
Dio2-R: 5'-CCCACCCACTCTCTGACTTTC-3'	Tsingke Biotechnology Co., Ltd.	N/A
Software and algorithms		
MATLAB	MathWorks	https://www.mathworks.com/products/matlab.html
LAS X	Leica	https://www.leica-microsystems.com/products/microscope-software/details/product/leica-las-x-ls/
ArControl behavioral system	Chen and Li[74]	N/A
Other		
Digital Stereotaxic Instruments	RWD Life Science Co.,Ltd. China	https://www.rwdstco.com/product-item/digital-stereotaxic-instruments/
Infrared thermograph camera (Fortric 225S)	Fortric, China	https://www.fotric.cn/products/23
Radiometer(SRC-200S)	Everfine Photo E Info CO., Ltd, China	http://www.everfine.net/en/productsinfo.php?cid=116&id=589
Leica SP8 scanning microscope	Leica, Germany	https://www.leica-microsystems.com.cn/cn/products/confocal-microscopes/p/leica-tcs-sp8/
Cryostat microtome	Leica, Germany	https://www.leicabiosystems.com/zh-cn/histology-equipment/cryostats/leica-cm3050-s/
Arduino Uno Rev3	Arduino, Italy	https://store.arduino.cc/products/arduino-uno-rev3
LightCycler-® 96 Instrument	Roche, Switzerland	https://sequencing.roche.com/us/en/products/group/lightcycler-96.html
Accu-Chek Aviva plus glucometer	Roche, Switzerland	https://www.accu-chek.com/meters/aviva-meter
Promethion Metabolic Cage System,	Sable Systems International, USA	https://www.sablesys.com/products/promethion-core-line/
AB Sciex 6500+ quadrupoleion trap mass spectrometer	AB Sciex, Framingham, MA, USA	https://sciex.com/products/massspectrometers/qtrap-systems/qtrap-6500plus-system
ExionLC™ AD ultra-highperformanceliquid chromatography	AB Sciex, Framingham, MA, USA	https://sciex.com/cr/products/hplc-products/ exionlc
Shim-pack GIST C18 column	Shimadzu, Columbia, MD, USA	227-30001-02
Sorvall™ ST 16 Centrifuge	Thermo Fisher Scientific Inc. USA	https://www.thermofisher.com/order/catalog/product/75004240?SID=srch-hj-75004240
NanoVue spectrophotometer	GE Healthcare, USA	https://www.gehealthcare.com/
Microliter Syringes (Model 65 removable needle with 31-gauge customized needle)	Hamilton company, USA	https://www.hamiltoncompany.com/laboratory-products/syringes/general-syringes/microliter-syringes
Dental cement	Super-Bond C&B, Sun Medical Co., Japan	https://sunmedical.co.jp/english/product/super-bond/cb-kit/index.html

RESOURCE AVAILABILITY

Lead contact

Further information and requests for resources and reagents should be directed to and will be fulfilled by the lead contact, Tian Xue (xuetian@ustc.edu.cn).

Materials availability

This study did not generate new unique reagents.

Data and code availability

- Blood glucose and iBAT thermogenesis raw data have been deposited at Mendeley Data and are publicly available as of the date of publication. Accession numbers are listed in the key resources table.
- This paper does not report original code.
- Any additional information required to reanalyze the data reported in this paper is available from the lead contact upon request

EXPERIMENTAL MODEL AND SUBJECT DETAILS

Human participants

The study was conducted according to the ethical guidelines of the First Affiliated Hospital of the University of Science and Technology of China and all the subjects signed informed consent to participate in the study (KY2022-046). During the daytime, for OGTT between the white light and darkness at ~19°C ambient temperature, 12 healthy individuals (6 males, 6 females) were recruited, with ages of 26.5 (SD±3.4) years and with BMI of 21.7 (SD±3.5) kg/m^2. During the daytime, for OGTT between the white light and darkness at ~29°C ambient temperature, 10 healthy individuals (5 males, 5 females) were recruited, with ages of 24.9 (SD±3.5) years and with BMI of 21.1 (SD±2.4) kg/m^2. During the daytime, for OGTT between the blue/red light and darkness at ~19°C ambient temperature, 14 healthy individuals (5 males, 9 females) were recruited, with ages of 23.5 (SD±1.9) years and with BMI of 21.0 (SD±2.2) kg/m^2. During the nighttime, for OGTT between the white light and darkness at ~19°C ambient temperature, 14 healthy individuals (8 males, 6 females) were recruited with ages of 23.4 (SD±2.2) years and with BMI of 21.8 (SD±2.6) kg/m^2. For more detailed information, see Supplemental Table (Table S1).

Animal

All experiments were performed with adult male mice (8-16 weeks, C57BL/6J or transgenic mice as specified) in this study. All mice were housed under a 12 h/ 12 h light/dark cycle (~100 lux white ambient illumination) and at an ambient temperature of 23°C ad libitum. All animal procedures were approved by the Institutional Animal Care and Use Committees at the University of Science and Technology of China (USTC) and the Chinese Academy of Sciences (CAS) review board. C67/BL6J mice were purchased from SPF (Beijing) Experimental Animal Science and Technology Co., Ltd. Cre recombinase-induced *Opn4* gene(Gene ID: 94233, encoding melanopsin) knockout (*Opn4*$^{f/f}$), *Opn4*^{Cre}, *Opn4* knockout (OPN4-KO, *Opn4*$^{-/-}$) and melanopsin-Only (MO: *Gnat1*$^{-/-}$, *Gnat1* encoding the rod specific α transducin; *Cnga3*$^{-/-}$, *Cnga3* encoding the cone specific cyclic nucleotide channel subunit; *Opn4*$^{+/+}$) mice were generous gifts from Ph.D. King-Wai Yau, Johns Hopkins University. Adrb3$^{-/-}$ (β3-adrenergic receptor (β3AR) knockout) mice were provided by Wen-Wen Zeng, Tsinghua University. *Avp-IRES2-Cre* mice (Stock No: 023530), *Oxt-IRES-Cre* mice (Stock No: 024234), *Vgat-IRES-Cre* knock-in mice (Stock No: 028862) and *Ai3* mice (Stock No: 007903) were obtained from Jackson Laboratories.

METHOD DETAILS

Light sources

Light intensity at the general room level usually ranged from 150 to 500 lux. We used sunlight, and white, blue and red LED light (~200-400 lux) as the light stimulus in this study. We detected their wavelength in nanometer (380nm-780nm) by a radiometer (SRC-200S, Everfine Photo-e-info CO., Ltd, China). To facilitate comparisons, the light source was converted to ''equivalent monochromatic 480 nm (peak spectrum of melanopsin) light'', by normalized Opn4 sensitivity spectrum,[22] $f(\lambda)$, and the measured spectrum of the light stimulus, $L(\lambda)$. The conversion formula is:

$$\text{Photons}_{equivalent\ 480nm\ light} = \int_{200nm}^{780nm} f(\lambda) * L(\lambda) d\lambda$$

The ambient sunlight intensity (8.80E+06 photons/um2.s) of testing room was measured on a clear day in Hefei Anhui during mid-afternoon. Given that the detection range of this radiometer (380 nm - 780 nm) does not completely contain ultraviolet (UV) light components, we revised the sunlight spectrum (200nm-780nm) using a standard spectrum from ASTM (G173-03 Standard Tables for Reference Solar Spectral Irradiances). The revised sunlight spectrum was converted to ''equivalent monochromatic 480 nm (peak spectrum of melanopsin) light'' using above formula.

Overall physical detection

To measure overall physical activity, beam-crossing monitoring was conducted using a Sable Systems (Promethion Metabolic Cage System, Sable Systems). In brief, mice were acclimated for 4 days in cages under a 12:12 light/dark cycle. Subsequently, mice were monitored for 24 h under 12:12 L/D ambient light, and then monitored for another 24 h with dark exposure from ZT5 to ZT8.5 or light exposure from ZT13 to ZT16.5.

Pupillary light reflex

Head-fixed mice were used for pupillary light reflex (PLR) experiments. One week before PLR experiments, mice were anesthetized with 1.5–2.0% isoflurane and a plastic head bar was secured to the skull using dental cement (Super-Bond C&B, Sun Medical Co., Japan). *Opn4*$^{+/+}$; *Pde6b*$^{rd1/rd1}$; *Cone*^{DTA} (only ipRGC photoreception) mouse was exposed to a 10 sec white light, blue light, sunlight or red light after 2 h dark adaptation. We measured the diameter of the pupil, using an infrared CCD camera. Videos were recorded at a frame rate of 5 Hz and analyzed using MATLAB software. The pupil area was measured at maximum constriction after light stimulation begin.

IPGTT and ITT

Mice were brought from the animal housing room into the testing room (12 h/ 12 h light/dark cycle) and acclimated for 2 weeks prior to testing. Each mouse underwent multiple IPGTT (Intraperitoneal glucose tolerance test) with an interval of 3-4 days between light (red/blue/white/sunlight) and dark. Especially for chemogenetic manipulation experiments, each mouse underwent forth IPGTT (light-PBS, light-CNO, dark-PBS, dark-CNO). During IPGTT, the blood samples were taken from tail vein nicks at 0 min (ZT7, when mice have been subjected to dark/light for 2 hr.) and at 15, 30, 60 and 90 min after glucose injection (i.p. 20% glucose solution, 1 g/kg). During the ITT, blood samples were taken at 0, 15, 30, 60, 90, 120, 150 and 180 min after insulin injection (ITT, i.p. 0.5 U/kg). To minimize stress from restriction of voluntary locomotor activities by handling, and to prevent intraperitoneal injection using needle during multiple ipGTT experiments, mice were head-fixed and placed on a single-axis rotating ball, on which they could run freely during ipGTT. Mice were anesthetized with 1.5–2.0% isoflurane, and a plastic head bar was secured to the skull using dental cement (Super-Bond C&B, Sun Medical Co., Japan). And then the sterile catheter was placed into the abdomen, and tunneled subcutaneously to the top of the neck and secured with dental cement, allowing for glucose or other agents loading to be done with no handling. After a 1-week surgical recovery, mice were habituated to head-fix and running on a free-spinning single-axis rotating ball for 1 week. Blood glucose was measured by using an Accu-Chek Aviva plus glucometer (Roche, Indianapolis, IN). The experimenter wore a red, low-illumination headlamp (illumination wavelength >650 nm and <10 lux) to operate per under dark conditions. We calculated the percent change in blood glucose relative to the baseline (time 0), and the area under the time curves (AUC) for percent change in blood glucose using the linear trapezoidal rule:

$$g_{time(i)} = \left[\left(G_{time(i)} \,/\, G_{time(0)} - 1\right) * 100\right]\%$$

$$AUC = \left[\sum_{i=1}^{n} \frac{g_{time(i)} + g_{time(i-1)}}{2} * \left(time_{(i)} - time_{(i-1)}\right)\right] \Big/ \left(time_{(n)} - time_{(0)}\right)$$

where $g_{time(i)}$ is the percent change in blood glucose, $G_{time(0)}$ is the glucose concentration at baseline and $G_{time(i)}$ is the glucose concentration at one of timepoints.

Stereotaxic injection

Adult mice were anesthetized with 1.5%–2.0% isoflurane (RWD Life Science Co., China) and fixed on a stereoscope apparatus (RWD Life Science Co., China). Erythromycin ointment (Jiangxi Decheng Pharmaceutical Co., Ltd) was applied to the surface of the eyeballs to keep the cornea moist. The experimenter used a scalpel to make a small incision in the scalp along the midline of the head to expose the skull. The surface of the skull was disinfected by an alcohol cotton ball. A small window was drilled into the skull surface of the target area and 50 to 150 nl of virus was injected bilaterally into the target area at a rate of 50 nl/min. The coordinates, defined as dorsal–ventral (DV) from the brain surface, anterior–posterior (AP) from bregma and medial–lateral (ML) from the midline, were as follows: SON (AP, -0.50 mm from bregma; ML, ±1.25 mm; DV, -5.25 mm); SCN (AP, -0.50 mm from bregma; ML, ±0.40 mm; DV, -5.60 mm; 2 ° inclined); PVN (AP, -0.60 mm from bregma; ML, ±0.25 mm; DV, -4.70 mm); NTS (AP, -7.80 mm from bregma; ML, ±0.50 mm; DV, -3.75 mm); RPa (AP, -7.60 mm from bregma; ML, 0.00 mm; DV, -5.40 mm). After the completion of injection, including a 10-min delay, the injection pipette was slowly withdrawn and the scalp was sutured back. Following surgery, mice were allowed to recover from anesthesia on a heating mat before being returned to their home cages.

Anterograde, retrograde tracing and virus

The following fluorescent tracing viral tools were employed in this study: AAV2/2-hEF1α-DIO-ChR2-eYFP (1E+13 V.G./ml) was used in intraocular injections to Cre-dependently express ChR2 and yellow fluorescence. AAV2/2Retro-hEF1a-DIO-ChETA-EYFP (1E+13 V.G./ml) was used to retrogradely express ChETA and yellow fluorescence in the neurons projecting to the injection site through terminal absorption. scAAV2/1-hSyn-Cre-pA (1E+13 V.G./ml) was used to express Cre recombinase in postsynaptic neurons to achieve input-specific labeling. AAV2/2Retro-hSyn-Cre (5E+12 V.G./ml) and AAV2/2Retro-hSyn-Flp (5E+12 V.G./ml) were used to retrogradely express Cre and Flp recombinase in the neurons projecting to the injection site through terminal absorption. AAV2/2Retro-CAG-FLEX-Flp (5E+12 V.G./ml) was used to retrogradely Cre-dependently express Flp recombinase in the neurons

projecting to the injection site through terminal absorption. AAV2/9-hEF1a-DIO-EYFP (1E+12 V.G./ml) and AAV2/9-CAG-FLEX-GFP (1E+12 V.G./ml) were used to Cre-dependently express fluorescence. AAV2/9-hEF1a-fDIO-mGFP (1E+12 V.G./ml) was used to Cre-dependently express green fluorescence. AAV2/9-GAD67-DIO-mCherry (1E+12 V.G./ml) was used to Cre-dependently express red fluorescence in inhibitory neurons. AAV2/9-hSyn-DIO-hM4Di-mCherry (1E+12 V.G./ml) and AAV2/9-hSyn-DIO-mCherry (1E+12 V.G./ml) were used to Cre-dependently express the inhibitory DREADD, and mCherry was used as a control in central neurons. AAV2/9-hEF1a-fDIO-hM4Di-mCherry (1E+12 V.G./ml) was used to Flp-dependently express the inhibitory DREADD in central neurons. AAV2/2-hSyn-DIO-hM3Dq-mCherry (1E+13 V.G./ml), AAV2/2-hSyn-DIO-hM4Di-mCherry (1E+13 V.G./ml) and AAV2/2-hSyn-DIO-mCherry (1E+13 V.G./ml) were used to Cre-dependently express excitatory DREADDs, the inhibitory DREADDs, and mCherry was used as a control in intraocular injections. AAV2/9-CAG-DIO-TetTox-EGFP (1E+12 V.G./ml) was used to Cre-dependently express the light chain of tetanus toxin (TetTox) in central neurons to block synaptic transmission. AAV2/5-hEF1a-DIO-RVG (2E+12 V.G./ml) was used to Cre-dependently express G protein, which reinstated the trans-synaptic capability of modified rabies virus (RV-EnvA-△G-mRuby3), and AAV2/5-hEF1a-DIO-H2B-EGFP-T2A-TVA (1E+12 V.G./ml) was employed to direct the infection of modified RV (RV-EnvA-△G-mRuby3). RV-EnvA-△G-mRuby3 (2E+8 TU/ml) was used in conjunction with the aforementioned helper viruses for retrograde trans-synaptic tracing. PRV-RFP (2E+9 PFU/ml) was used for polysynaptic retrograde tracing from intrascapular brown adipose tissue (iBAT).

AAV2/2Retro-hEF1a-DIO-ChETA-EYFP was prepared in the Xue laboratory. AAV2/9-GAD67-DIO-mCherry was obtained from OBiO Technology (Shanghai) Corp., Ltd. All other AAV tools and RV-EnvA-△G-mRuby3 were obtained from Shanghai Taitool Bioscience Co., Ltd. PRV-RFP was obtained from BrianVTA (Wuhan) Co., Ltd.

SCN and SON extatory toxin lesion

For excitotoxicity experiments, we injected bilaterally a 30 nl NMDA (50 mM) solution into the SON or SCN. The injection process was the same as described above. Finally, glial fibrillary acidic protein (GFAP) staining and wheel running tests were used to verify the lesion effect. We conducted follow-up intraperitoneal glucose tolerance Test (ipGTT) experiments two weeks after NMDA injection.

DREADDS

DREADDs (designer receptors exclusively activated by designer drugs) strategy. In this study, we manipulated neural circuits using hM3D (Gq) for activation and hM4D (Gi) for inhibition. Thirty minutes prior to IPGTT, CNO (Clozapine-N-Oxide, Sigma-Aldrich St. Louis, MO, USA) was intraperitoneally (i.p.) injected (2 mg/kg).

Intraocular injection

A dilating eye drop (1% w/v Atopin and 5% w/v phenylephrine hydrochloride) was applied to dilate the pupils. After approximately 5 min or until the pupils were fully dilated, mice were anesthetized with 1.5%–2.0% isoflurane, and eye gel (5% sodium carboxymethyl cellulose) was used to prevent eyes from drying. The eyeball was then penetrated through the pupil with the tip of a 26-gauge needle under the stereoscope to release the ocular pressure, immediately followed by the bilateral injection of 1.5 μl of virus (1E+13 V.G./ml) or tracing dye into the vitreous chamber (the space between the lens and the retina) of the eyes, to ensure delivery specifically to the retina, using a Hamilton syringe (Model 65 RN SYR with 31-gauge customized needle). Following surgery, mice were allowed to recover from anesthesia on a heating mat before being returned to their home cages, and those with noticeable bleeding or damage to the retina were excluded from further experiments.

Wheel running test

All mice were individually housed in cages equipped with a running wheel (110 mm diameter). LED lights (~200 lux, illumination wavelength 410–720 nm) with adjustable brightness were installed at the top of each cage. All animals were housed at room temperature with ad libitum access to food and water. The number of wheel revolutions was counted using a custom-made drive based on ArControl.[74] The activity distribution in 5 min time bins was analyzed using MATLAB software.

Metabolic profiling analysis

Serum samples were collected via the ocular vein after 2.5 h of fasting with or without light exposure during the daytime. The blood was centrifuged (1500 rpm, 15 min) for serum, quickly frozen with liquid nitrogen, and then stored at -80°C for subsequent testing. The experimenter wore a red, low-illumination headlamp (illumination wavelength >650 nm and <10 lux) to operate under dark conditions. To screen the changes in serum nutrients between light/dark conditions, untargeted metabolomics using UHPLC (1290 Infinity II, Agilent Technologies) coupled to a quadrupole time-of-flight (AB Sciex TripleTOF 6600) was executed at Shanghai Applied Protein Technology Co., Ltd. The aforementioned serum samples (100 μl) were added 4 volumes of cold methanol/acetonitrile (1:1, v/v) and the mixtures were centrifuged for 20 mins (14000g, 4°C). The supernatant was collected and dried in a vacuum centrifuge. For liquid chromatography (LC) mass spectrometry (MS) analysis, the samples were re-dissolved in 100 μl acetonitrile/water (1:1, v/v) solvent. To monitor the stability and repeatability of instrument analysis, quality control (QC) samples were prepared by pooling 10 μl of each sample and analyzed together with the other samples. The blank sample was the mobile phase A (25 mM ammonium acetate and 25 mM ammonium hydroxide in water). All samples (experimental samples, QC samples, and blank samples) were injected into UHPLC system. The QC samples were inserted regularly and analyzed in every five samples. Then all samples and

the QC sample were separated on a hydrophilic interaction chromatography column (Waters, ACQUITY UPLC BEH Amide 1.7 μm, 2.1 mm× 100 mm column), in both ESI positive and negative modes. The mobile phase contained A=25 mM ammonium acetate and 25 mM ammonium hydroxide in water and B= acetonitrile. The gradient was 95% B for 0.5 min, linearly reduced to 65% in 7 min, reduced to 40% in 0.1 min and kept for 1 min, and then increased to 95% in 0.1 min, with a 3 min re-equilibration period employed. The product ion scan was acquired using information dependent acquisition with high sensitivity mode selected. After peak picking and grouping, all sample values were normalized to total peak intensity. In the extracted ion features, only the variables having more than 50% of the nonzero measurement values in at least one group were kept. Compound identification of metabolites by MS/MS spectra with an in-house database established with available authentic standards. Student's *t*-tests at univariate level were used to measure the significance of each metabolite, and p values less than 0.05 were considered statistically significant.

A panel of hormones associated with glucometabolism, were detected by ELISA. The ELISA kits used in this study were as follows: Insulin ELISA kit (Millipore, EZRMI-13K); Epinephrine ELISA kit (Elabscience, E-EL-0045c); Norepinephrine ELISA Kit (Elabscience, E-EL-0047c); Cholecystokinin ELISA kit (Cloud-Clone, CEA802Mu); Corticosterone ELISA Kit (Elabscience E-EL-0161c); Glucagon ELISA Kit (Elabscience E-EL-M0555c); Glucagon Like Peptide 1 ELISA Kit (Elabscience E-EL-M3012); Ghrelin ELISA Kit (Elabscience E-EL-M0551C); Orexin A ELISA Kit (Elabscience E-EL-M0860c); and Growth Hormone (Elabscience E-EL-M0060c). Nonesterified fatty acids (Elabscience E-BC-K013-S) and lactate (Elabscience E-BC-K044-M) were detected by colorimetric kits.

Radioimmunoassay and LC-MS/MS

Blood was collected via the ocular vein after 2.5 h of fasting with or without light exposure during the daytime. The blood was centrifuged (1500 rpm, 15 min) to obtain plasma, which was quickly frozen with liquid nitrogen, and then stored at -80°C. After all samples were collected, the plasma oxytocin was detected by LC-MS/MS and plasma vasopressin were detected by radioimmunoassay (RIA kit: KIPERB319, DIAsource ImmunoAssays S.A.). For LC–MS/MS, a 30 μL of plasma oxytocin was injected into an ExionLC™ AD UHPLC (AB SCIEX) and separated on a Shim-pack GIST C18 column (2 μm, 50 × 2.1 mm) (Shimadzu) with a flow rate of 0.4 ml/min at 40°C. Mobile phase A was water and mobile phase B was ACN. It was started with 5% mobile phase B for 0.5 min, then increased to 60% within 1 min, kept constant at 60% for 2 min, reduced to 5% at 4 min, and kept constant until the end of the run at 8 min. Autosampler temperature was kept at 10°C. The LC eluent was introduced into an AB Sciex 6500+ quadrupole ion trap mass spectrometer (AB Sciex, Framingham, MA, USA) for MRM using positive ion mode with ESI. The final MRM parameters were as follows: curtain gas (20 psi), collison gas (high), IonSpray voltage (5500 V), source temperature (550°C), ion source gas 1 (50 psi), ion source gas 2 (50 psi), declustering potential (60 V), and entrance potential (5 V). Quantification was performed by MRM of the protonated precursor molecular ions [M + H] + and the related product ions. The resolutions of the quadrupole Q1 mass (precursor ion) and Q3 mass (product ion) were set at high. For the MRM scan of OXT, ion pairs 1007.4 → 723.4 m/z were monitored for quantitation, while ion pairs 1007.4 → 285.0 m/z were monitored for confirmation. Chromatograms and mass spectral data were acquired and processed using Analyst®1.6.3 software (AB Sciex, Framingham, MA, USA).

Immunohistochemistry

Mice were anesthetized with 1.5%–2.0% isoflurane, and then PBS and 4% paraformaldehyde (PFA, w/v in PBS) solutions were infused intracardially. The brains were removed and postfixed in 4% PFA at 4°C for 24 h. The slices were dehydrated with 30% sucrose solution at 4°C for 24 h. Coronary slices of 40 um thickness were cut with a Cryostat microtome (Leica CM3050S) and the slices were washed with PBS (4*10 min). The tissues were blocked with blocking solution (PBS containing 5% BSA, 5% goat serum and 0.5% Triton X-100 as appropriate) at room temperature for 2 h. Then the sections were incubated with the primary antibody working solution (diluted with blocking solution) at 4°C for 48 h. The primary antibodies used in this study were as follows: rabbit anti-GFAP (Sangon Biotech D120691; 1:200); rabbit anti-c-Fos (Synaptic Systems 226003; 1:5,000; RRID AB_2231974; lot no. 7-78); rabbit anti-melanopsin (Advanced Targeting System, AB-N38, 1:10000; RRID AB_1266797; lot no. 112-16); rabbit anti-vasopressin (Immunostar #20069 1:500 RRID: AB_572219); rabbit anti-oxytocin (Abcam ab212193;1:500); and mouse anti-BDNF (Proteintech 66292-1-Ig; 1:200). After 48 h, the sections were washed with PBS (3*10 min). Then the working solution of the secondary antibody (diluted with blocking solution; 1:500) was incubated at room temperature for 2 h. The working solution of the secondary antibody used in this study was as follows: goat anti-rabbit Alexa Fluor 568 (Thermo Fisher A-11036, 1:500; RRID AB_10563566; lot no. 2155282), goat anti-rabbit Alexa Fluor 488 (Thermo Fisher A-11034, 1:500; RRID AB_2576217; lot no. 2069632) and donkey-anti-mouse Alexa Fluor 488 (Thermo Fisher A-10680, 1:500; RRID AB_2534062; lot no. 2318435).

For retinal immunohistochemistry, the eyes of the anesthetized mice were removed and fixed in 4% PFA for 24 h. The lens and RPE were then stripped, and filaments in the retina were cleaned. All staining procedures were performed according to the standard procedure mentioned above. All stained sections were photographed using a Leica confocal microscope (SP8, Leica).

Polysynaptic retrograde tracing

For polysynaptic retrograde tracing from intrascapular brown adipose tissue (iBAT), the two brown fat pads of mice were injected at 6 sites, each with 200 nL PRV-CAG-RFP (BrainTVA, Wuhan). Mice were infused intracardially with PBS and 4% paraformaldehyde (PFA, w/v in PBS) and photographed using a Leica confocal microscope (SP8, Leica) 6-8 days after the injection of PRV-RFP.

Molecular profiling of IBAT tissue

Mice were brought from the animal housing room into the testing room (12 h/ 12 h light/dark cycle) and acclimated for 2 weeks prior to testing. During testing, mice were fasted and pre-exposed to dark or light for 2 h (starting at ZT5) before glucose injections (ZT7). Then, mice were anesthetized with isoflurane at 0min (ZT7) and 30 min (ZT7.5) after glucose loading (1 g/kg), and rapid intra-cardiac perfusion was performed with ice-cold PBS. iBAT was removed, quickly frozen with liquid nitrogen and then stored at -80°C for subsequent testing. The experimenter wore a red, low-illumination headlamp (illumination wavelength >650 nm and <10 lux) to operate under dark conditions. Total RNA was isolated from iBAT tissue using TRIzol Reagent (Thermo Fisher), and the procedures for separating and purifying RNA were as follows: chloroform (200 ul/sample) was added, oscillated, incubated for 3 min, and centrifuged at 4°C (12000 g, 4 min). The upper transparent aqueous phase liquid was transferred to a new EP tube, and isopropyl alcohol (500 ul/sample) was added to the tube and evenly mixed. After standing for 20 min, the liquid was centrifuged at 4°C (12000 g, 15 min). The supernatant was discarded, and the pellet was washed by adding 1 mL ethanol solution (75%, cooled), evenly mixing, and centrifuging at 4°C (12000 g, 2 min). Finally, the RNA was dissolved in DEPC water. RNA quantity was measured with a NanoVue spectrophotometer (GE Healthcare, Little Chalfont, Buckinghamshire, UK). Reverse transcription was performed using the AG Evo M-MLV RT kit (Hunan Accurate Biotechnology Co.,Ltd). Quantitative, real-time PCR (qPCR) was performed using SYBR Green (Roche, Indianapolis, IN). Primers were used at a final concentration of 1 μM. Gene expression was normalized to the housekeeping gene GAPDH. The primers used in the study were as follows:

Gapdh: Forward: CTGCCCAGAACATCATCCCT.
Gapdh: Reverse: TGAAGTCGCAGGAGACAACC.
Ucp1: Forward: AAGCTGTGCGATGTCCATGT.
Ucp1: Reverse: AAGCCACAAACCCTTTGAAAA.
Pgcla2: Forward: AGCCGTGACCACTGACAACGAG.
Pgcla2: Reverse: GCTGCATGGTTCTGAGTGCTAAG.
Dio2: Forward: GTCCGCAAATGACCCCTTT.
Dio2: Reverse: CCCACCCACTCTCTGACTTTC.

Infrared thermograph

Mice were brought from the animal housing room into the testing room (12 h/ 12 h light/dark cycle) and acclimated for 2 weeks prior to testing. During testing, mice were fasted and pre-exposed to dark or light for 2 h (starting at ZT5) before glucose injections (ZT7). Then, an infrared thermograph camera (Fortric 225S) was used to detect the surface temperature above iBAT from a top view at 0 min (ZT7) and 30 min (ZT7.5) after glucose loading (1 g/kg) under light or dark conditions. Each time the camera was placed at the same distance from the mice to ensure that a clear image of the mouse body outline and hair could be obtained. The heatmaps were automatically generated by the camera software. The experimenter wore a red, low-illumination headlamp (illumination wavelength >650 nm and <10 lux) to perform experiments under dark conditions.

Human OGTT

Healthy volunteer subjects were recruited for a 75 g OGTT at ~19°C or ~29°C ambient temperature. Subjects underwent the OGTT twice or thrice with an interval of 3 days between the light (white/blue/red) and dark conditions. For human OGTT, the BMI, age and sex of each testees were recorded. Testees underwent overnight fasting when OGTT was performed during the daytime (08:00 to 12:00) and 8 h of fasting when OGTT was performed at nighttime (18:00 to 22:00). Testees sat on their own comfortable sofas, did not exercise and kept quiet in the room. The first 2 h of OGTT was for adaptation. The basal blood glucose concentration was measured first from finger blood. Then the testees took an oral glucose solution (150 ml medical 50% glucose solution diluted with purified water to 300 mL) and further blood samples were measured at 30, 60, 90 and 120 min using an Accu-Chek Aviva plus glucometer (Roche, Indianapolis, IN). The human OGTT data were statistically analyzed in the same way as the data from mouse IPGTT.

QUANTIFICATION AND STATISTICAL ANALYSIS

Randomization and blinding

In all experiments, the experimental animals were randomly assigned from multiple cages. The experimental animals were tested according to the semi-random principle, and the experimental and control animals were tested in turn. In all experiments involving the comparison between the light and dark conditions, the light or dark conditions were randomly tested in order. The experimenters were not completely blind when collecting data and grouping animals, as they needed to record the label of each animal and sample. However, each data was analyzed using consistent parameters and algorithms by nonparticipants.

Statistics reproducibility

Data are presented as the mean ± SEM. No statistical methods were used to predetermine sample sizes. Sample sizes are indicated in the figure' legends and associated text. Statistical differences of normally distributed data were determined using paired or unpaired two-tailed Student's t-test, or with two-way ANOVA statistical tests, followed by Tukey's post hoc test. P values less than 0.05 were considered significant. ns: not significant. P values are indicated as follows: * $P < 0.05$, ** $P < 0.01$, *** $P < 0.001$.

Supplemental figures

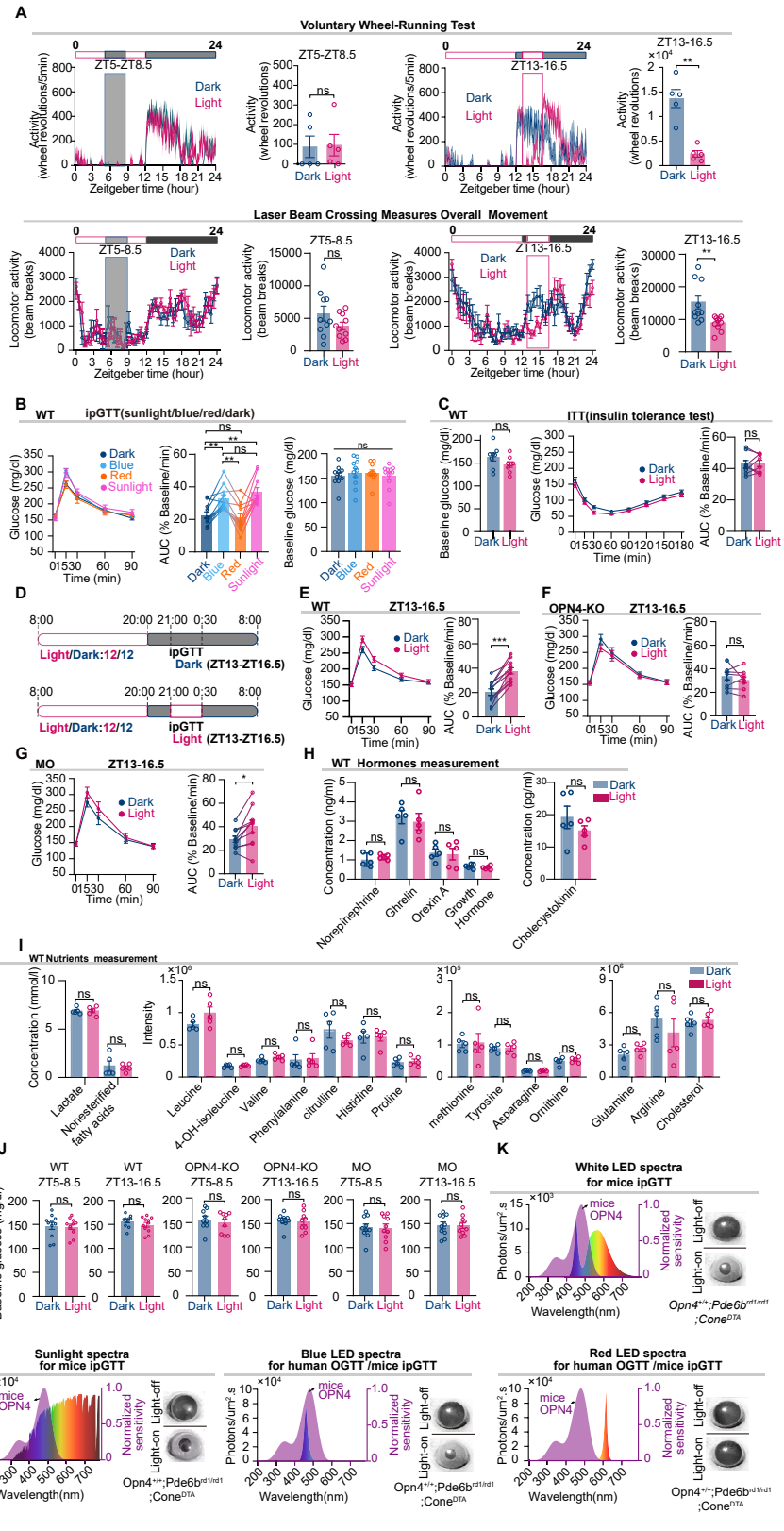

(legend on next page)

Figure S1. Light decrease GT at nighttime, related to Figure 1

(A) Upper: the mean number of wheel revolutions per 5 min for light/dark conditions during ZT5–ZT8.5 (left) or ZT13–ZT16.5 (right). n = 5 animals/group. By two-tailed non-paired t test. Lower: the total locomotor activity during ZT5–8.5 and ZT13–16.5. n = 10 mice/group. By two-tailed paired t test.

(B) Baseline concentrations and GT evaluation under the sunlight/blue/red (n = 11). By one-way ANOVA, Tukey's multiple comparisons test.

(C) Insulin tolerance test (i.p. 0.5 U/kg) between light/dark conditions. Insulin tolerance evaluation in WT mice (n = 8). Two-tailed paired t test.

(D–G) Schematic of IPGTT protocol during nighttime (D, ZT13–16.5). GT evaluation in WT mice (E, n = 11), in OPN4-KO mice (F, n = 9), and in MO mice (G, n = 10). All by two-tailed paired t test.

(H and I) Levels of glucometabolism-relevant hormones or nutrients under light/dark conditions. n = 5 mice/group. Two-tailed non-paired t test.

(J) Baseline concentrations of glucose in WT, OPN4-KO, or MO mice. Two-tailed paired t test.

(K and L) The normalized spectral sensitivity of mice OPN4 (purple), the spectrum of white/blue/red/sunlight. Blue, white, and sunlight, but not red, triggered pupil constriction in *Opn4*$^{+/+}$; *Pde6b*$^{rd1/rd1}$; *Cone*^{DTA} mice (only ipRGC photoreception).

*p < 0.05, **p < 0.01, and ***p < 0.001. Data were represented as mean ± SEM.

All by two-tailed paired t test.

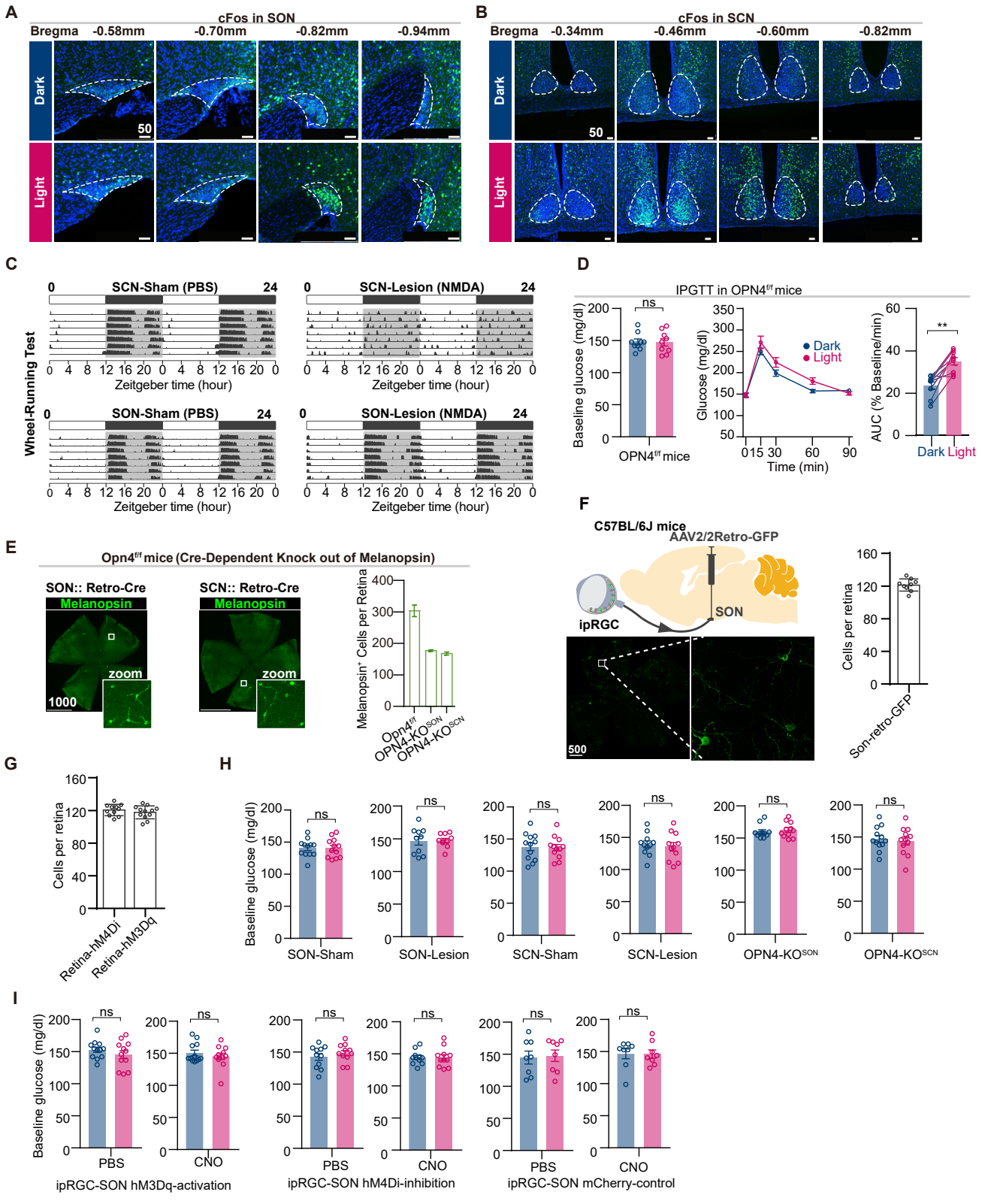

(legend on next page)

Figure S2. Wheel-running test in SCN-lesioned and SON-lesioned mice, related to Figure 2

(A and B) cFos expression elicited by light stimulation in the SON (A) and SCN (B).

(C) Wheel-running test for SCN-lesioned and SON-lesioned mice. SCN-lesioned mice lacked circadian rhythmicity.

(D) GT evaluation in *Opn4*$^{f/f}$ mice (n = 9). Two-tailed paired t test.

(E) Image of ipRGCs cells in retina of *Opn4*$^{f/f}$ mice. Quantification of ipRGCs cells after specific melanopsin knockout in SON-innervating ipRGCs (n = 177.2 ± 2.8, 11 mice), in SCN-innervating ipRGCs (n = 167.7 ± 4.8, 12 mice), or in control group (n = 303.8 ± 17.9, 9 mice). Thus, the achieved melanopsin knockout cells were ~126.6 and ~136.1 for OPN4-KO^{SON} and OPN4-KO^{SCN} mice, respectively.

(F) Schematic of retina retrogradely labeled experiment by injecting AAV2/2Retro-GFP into SON. Targeted cells per retina in this retrogradely labeled experiment (mean ± SD,121.3 ± 7.5, n = 9).

(G) Targeted cells per retina in hM4Di (mean ± SD, 120.6 ± 7.0, n = 11) and hM3Dq (mean ± SD, 117.8 ± 7.9, n = 12) experiments.

(H and I) Baseline concentrations of glucose in SON-Sham, SON-Lesion, SCN-Sham, SCN-Lesion, and retina hM3Dq, retina hM4Di, and retina mCherry experiments. Two-tailed paired t test.

*$p < 0.05$, **$p < 0.01$, and ***$p < 0.001$. Data were represented as mean ± SEM. Scale bars, 50 μm in (A and B), 1,000 μm in (E), and 500 μm in (F).

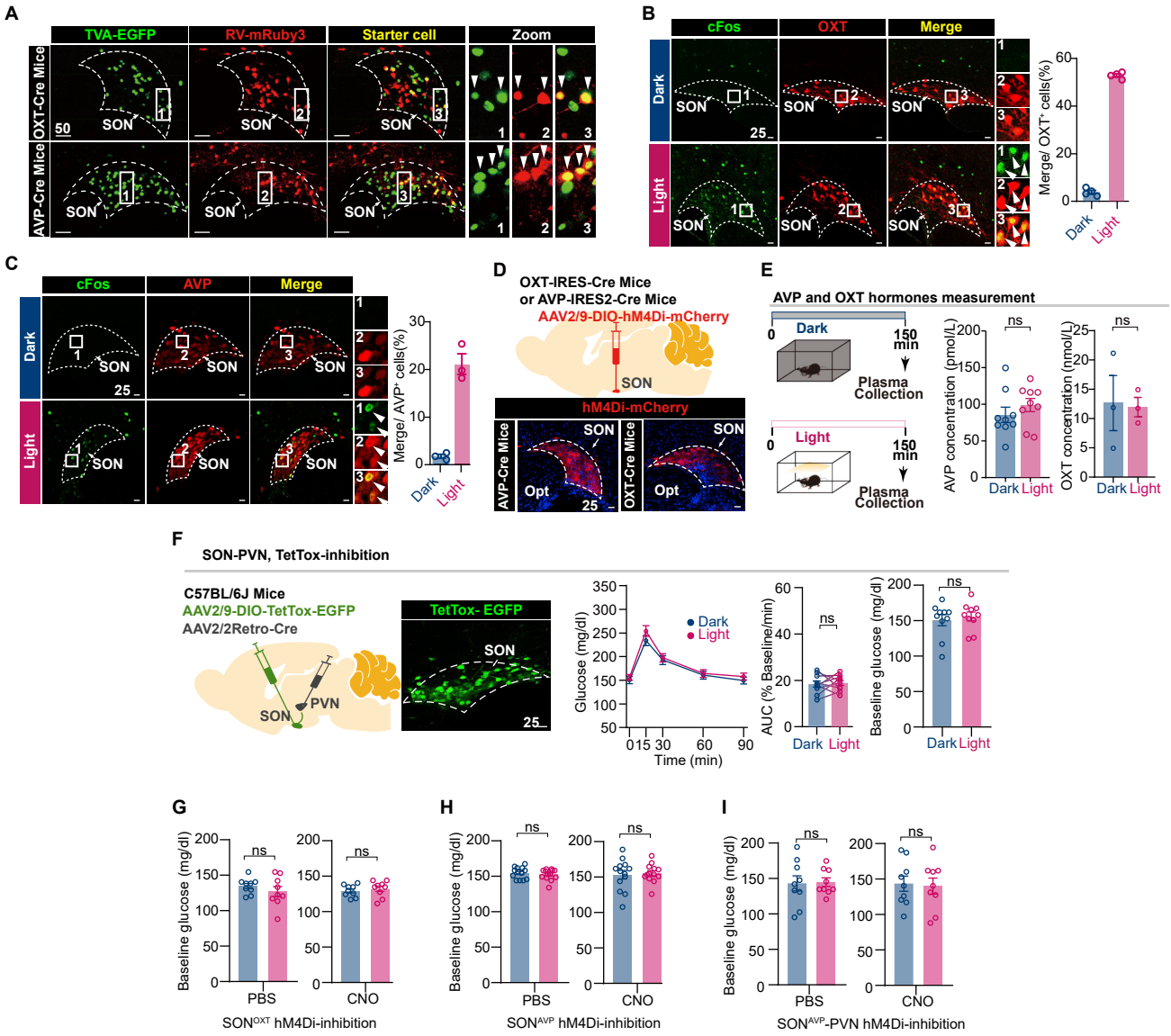

Figure S3. Light do not alter plasma AVP and OXT hormones level, related to Figure 3

(A) Experiment of monosynaptic tracing showing starter cells (yellow) in the SON area (red, RV; green, helper viruses) of *Oxt-Cre* (top) or *Avp-Cre* mice (bottom).
(B and C) Representative images of cFos immunofluorescence and close-up showing co-localization of cFos (green) with SON^{OXT} neurons (red) in *Oxt-Ai3* mice (B) or of cFos (green) with SON^{AVP} neurons (red) in *Avp-Ai3* mice (C), using light stimulation. Percentage of $cFos^{+}$-OXT^{+} neurons in OXT^{+} or AVP^{+} neurons (light versus dark: 52.9% ± 0.35% versus 3.86% ± 0.90% for OXT neurons, n = 4 mice/group; 21.1% ± 2.1% versus 1.78% ± 0.41% for AVP neurons, n = 3 mice/group).
(D) Schematic and image of chemogenetic inhibition of SON^{AVP} or SON^{OXT} neurons.
(E) Experimental procedures for measuring plasma AVP level (n = 9 mice/group) and plasma OXT level (n = 3 mice/group) between light/dark conditions. Both by two-tailed non-paired t test.
(F) GT evaluation in TetTox-mediated inhibition of SON-PVN pathway (n = 10 mice). Two-tailed paired t test.
(G–I) Baseline concentrations of glucose in hM4Di experiments for SON^{OXT}, SON^{AVP}, and SON^{AVP}–PVN pathway. Two-tailed paired t test.
*p < 0.05, **p < 0.01, and ***p < 0.001. Data were represented as mean ± SEM. Scale bars, 50 μm in (A) and 25 μm in (B, C, D, and F).

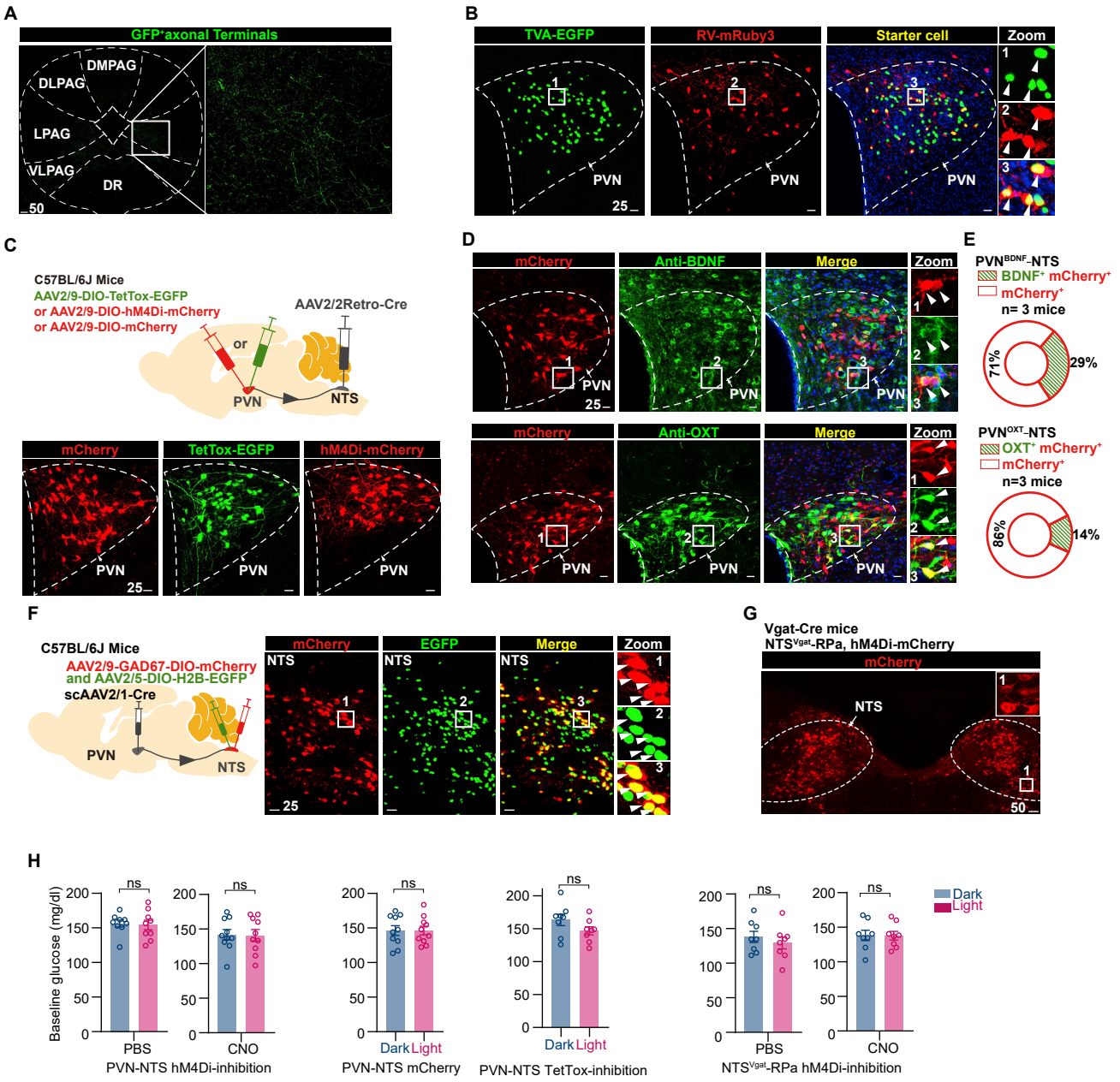

Figure S4. SON-innervated PVN neurons sparsely innervate PAG and DR, related to Figure 4

(A) Terminal field of SON-innervated PVN neurons in the PAG and DR regions. DMPAG, dorsomedial periaqueductal gray; DLPAG, dorsolateral periaqueductal gray; VLPAG, ventrolateral periaqueductal gray; LPAG, lateral periaqueductal gray; and DR, dorsal raphe nucleus.

(B) Experiment of monosynaptic tracing in NTS-projecting PVN area showed starter cells (yellow) in the PVN area (red, RV; green, helper viruses).

(C) Schematic and image of selective inhibition of NTS-projecting PVN neurons.

(D and E) The retrograde tracing experiment was used to identify the NTS-projecting PVN neuron types (D). Percentage (E) of BDNF^{+} (29.1% ± 4.3%) or OXT^{+} (14.5% ± 0.79%). n = 3 mice/group.

(F) Schematic of the anterograde trans-synaptic tracing showing co-localization (yellow) of PVN-projected NTS neurons (green) with GABAergic neurons (red).

(G) Image of selective inhibition of RPa-projecting NTS^{Vgat} neurons.

(H) Baseline concentrations of glucose in PVN-NTS hM4Di, PVN-NTS mCherry, PVN-NTS TetTox, and NTS^{Vgat}–RPa experiments. Two-tailed paired t test. Data were represented as mean ± SEM. Scale bars, 50 μm in (A and G) and 25 μm in (B, C, D, and F).

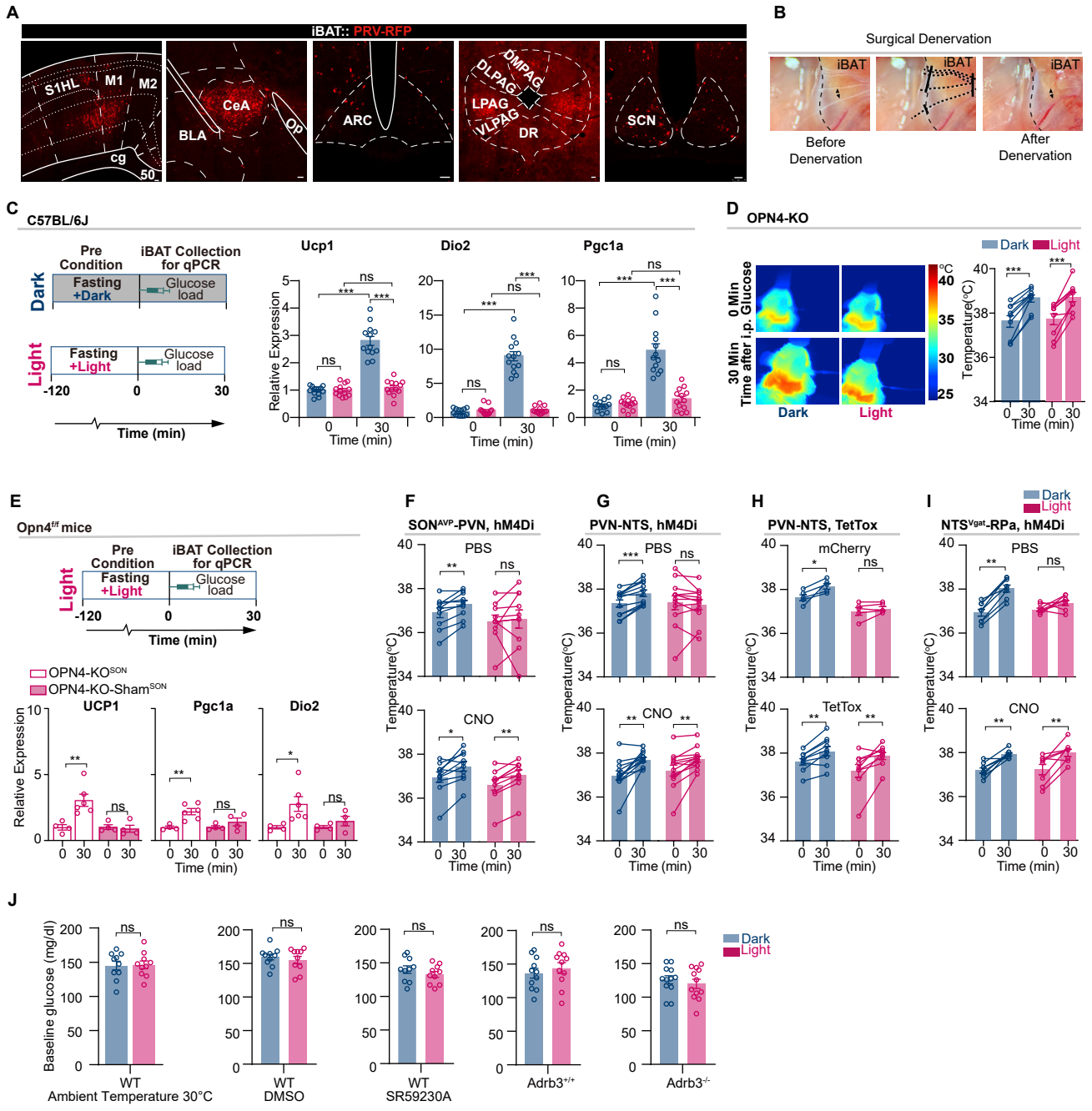

Figure S5. Light represses the expression of thermogenic genes in iBAT via ipRGC-SON pathway, related to Figure 5

(A) Representative images showing RFP$^+$ neurons in primary motor cortex (M1), central amygdala (CEA), arcuate nucleus (ARC), periaqueductal gray (PAG), dorsal raphe (DR), and suprachiasmatic nucleus (SCN) that were polysynaptically linked to iBAT.

(B) Representative image showing five branches of intercostal nerves before and after surgical denervation.

(C) Experimental procedures for measuring *Ucp1*/*Pgc1a*/*Dio2* in iBAT at 0 min (ZT7, when mice have been subjected to dark/light for 2 h) and at 30 min (ZT7.5) after glucose loading. n = 13 mice/group. One-way ANOVA, Tukey's multiple comparisons test.

(D) iBAT surface temperature in OPN4-KO mice (n = 9). Two-tailed paired t test.

(E) Expression of thermogenic genes in light conditions of OPN4-KO^{SON} (at 0 min, n = 4; at 30 min, n = 6) or OPN4-KO-Sham^{SON} (n = 4 mice/group) mice. Two-tailed non-paired t test.

(F–I) iBAT surface temperature measurement with CNO-induced inhibition of SON^{AVP}-PVN (F, n = 9 mice), of PVN-NTS (G, n = 12 mice), and of NTS^{Vgat}-RPa (H, n = 8 mice), and with TetTox-mediated inhibition of PVN-NTS (I, n = 5 for mCherry, n = 9 for TetTox). All by two-tailed paired t test.

(legend continued on next page)

(J) Baseline concentrations of glucose in WT at thermoneutrality, WT with DMSO treatment, WT with SR59230A treatment, *Adrb3*$^{-/-}$ littermate control (*Adrb3*$^{+/+}$), and *Adrb3*$^{-/-}$ experiments. Two-tailed paired t test.

Pgc1a, peroxisome proliferator-activated receptor gamma coactivator 1-alpha; Dio2, type II iodothyronine deiodinase; Ucp-1, uncoupling protein 1.

*$p < 0.05$, **$p < 0.01$, and ***$p < 0.001$. Data were represented as mean ± SEM. Scale bars, 50 μm in (A).

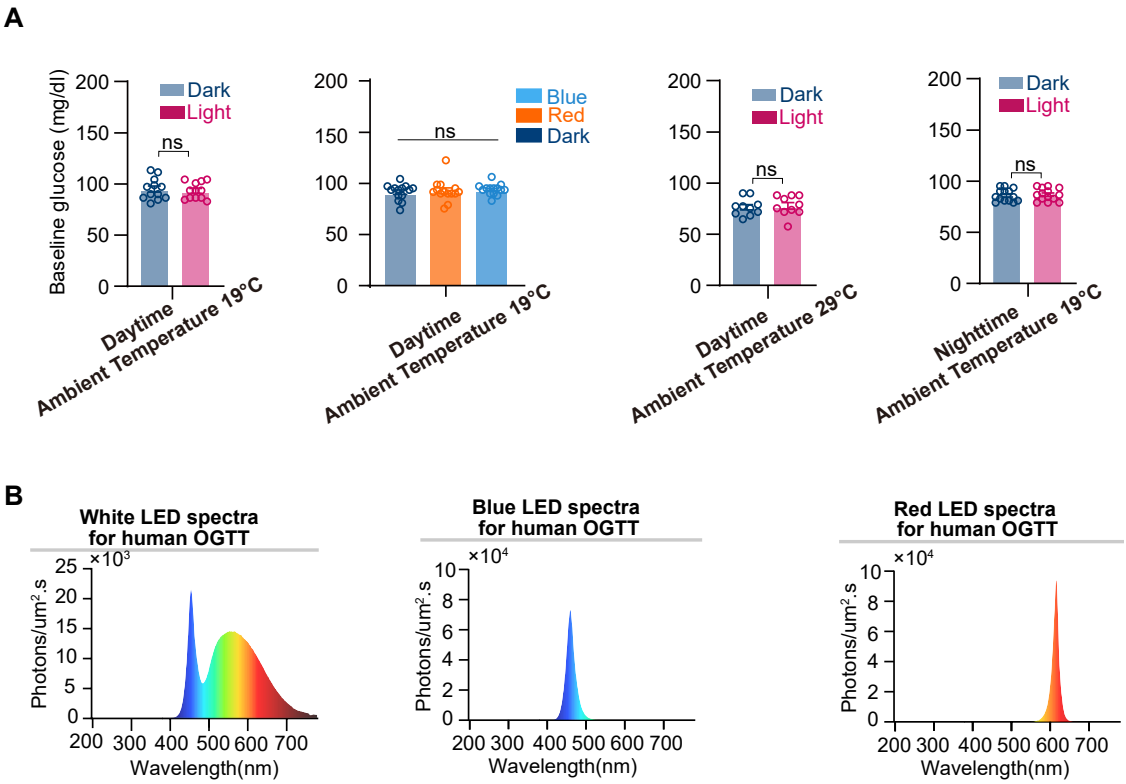

Figure S6. Basal glucose in human OGTT, related to Figure 6

(A) Baseline concentrations of glucose in human OGTT. Two-tailed paired t test.

(B) The spectrum of white, blue, and red light during human OGTT.

*p < 0.05, **p < 0.01, and ***p < 0.001. Data were represented as mean ± SEM.